The T-Bird – A new aircraft-towed instrument platform to measure ~~turbulence and~~ aerosol properties and turbulence close to the surface: Introduction to the aerosol measurement system~~.~~

Zsófia Jurányi[1], Christof Lüpkes[1], Frank Stratmann[2], Jörg Hartmann[1], Jonas Schaefer[2], Anna-Marie Jörss[1], Alexander Schulz[1], Bruno Wetzel[2], David Simon[2], Eduard Gebhard[1], Maximilian Stöhr[1], Paula Hofmann[1], Dirk Kalmbach[1], Sarah Grawe[2], Manfred Wendisch[3], and Andreas Herber[1]

[1]Alfred Wegener Institute, Helmholtz Centre for Polar and Marine Research, Bremerhaven, Germany
[2]Leibniz-Institute for Tropospheric Research, Leipzig, Germany
[3]Leipzig Institute for Meteorology, University of Leipzig, Leipzig, Germany

Correspondence: Zsófia Jurányi (zsofia.juranyi@awi.de)

Abstract. This study introduces the T-Bird, a novel aircraft-towed platform developed to measure ~~turbulence and aerosol~~ aerosol and turbulence properties close to the surface, particularly over sea ice and open water in the polar regions. The T-Bird~~system~~, towed by the Alfred Wegener Institute's Polar aircraft, offers a unique capability to capture data from altitudes as low as $\sim$10 m while the aircraft operates at its lowest allowed operation altitude. This measurement platform allows for simul-
5 taneous data collection of ~~turbulence, aerosol, and other atmospheric~~ aerosol, turbulence, and meteorological parameters across multiple vertical layers. The T-Bird is equipped with specialized aerosol instrumentation to assess particle number concentration, number size distribution, and absorption coefficient and to collect filter samples. It has been tested under Arctic conditions during the BACSAM (Boundary layer and Aerosol and Cloud Study in the Arctic, based on aircraft and T-Bird Measurements) campaign in October 2022. This paper provides technical details on the T-Bird's design, with special focus on the aerosol
10 instrumentation, and its performance during Arctic flights addressing measurement challenges in the lowermost atmosphere. The first measurements demonstrate its potential to enhance our understanding of aerosol dynamics and atmospheric boundary layer processes in remote environments.

1 Introduction

Aerosols play a crucial role in ~~Earth's radiative energy balance~~ atmospheric radiative energy budget and climate, directly by
15 scattering and absorbing solar radiation, and indirectly by modifying cloud microphyisical properties (e.g. Szopa et al., 2021). The global warming due to the increase of greenhouse gas concentrations is ~~accelerated~~ amplified in the Arctic (Jeffries et al., 2013; AMAP, 2021) as ~~the result of the action of a multitude of~~ a result of various of processes and feedback mechanisms summarized by the term of Arctic amplification (e.g. Wendisch et al., 2017). One of these interactions within the Arctic climate system is related to changes of aerosol concentrations (AMAP, 2021). The natural aerosol baseline in the Arctic is changing
20 rapidly, accompanied by significant regional variations. The majority of Arctic aerosols originate from sources at lower latitudes

traveling long distances through the atmosphere (Barrie et al., 1992). However, the recently growing human influence in the Arctic accentuates the significance of local ~~pollutant~~ pollution sources as well (Law et al., 2017). Altogether, the role of long-range transported or locally emitted aerosol particles in Arctic amplification, particularly aerosol-cloud interaction, is complex and still not well understood (Mauritsen et al., 2011; Pithan and Mauritsen, 2014; Wendisch et al., 2017). In this regard, more measurements are required to improve our understanding of aerosol effects (e.g. Schmale et al., 2021).

Limited accessibility, harsh weather conditions, and the vastness of the Arctic complicate long-term and comprehensive aerosol measurements. Nevertheless, several ground-based research stations and monitoring sites have been established since the 1970s to collect continuous, long-term aerosol data. Some of the oldest stations are Barrow/Utqiaġvik (Bodhaine, 1989; Polissar et al., 1999), situated in Alaska, and Zeppelin in Ny-Ålesund, Svalbard (Platt et al., 2022). In the 1980s Alert station in Canada (Sirois and Barrie, 1999) and Villum Research Station in Greenland (Heidam et al., 1999; Nguyen et al., 2016) have started their operations in the high Arctic. These ground-based ~~stations~~ sites provide valuable information on the seasonal variations and long-term trends of aerosol properties. However, these ~~provide data~~ data are limited to single geographic points on the ground.

Ship-based aerosol measurements can cover wide ranges of oceanic, sea-ice and coastal regions, providing a more extensive and diverse sampling of the Arctic environment (e.g. Chang et al., 2011; Tjernström et al., 2014; Wendisch et al., 2019). The most comprehensive atmospheric measurement program conducted over the Arctic sea ice to date was part of the MOSAiC (Multidisciplinary drifting Observatory for the Study of Arctic Climate) campaign, which provided year-around, continuous aerosol observations from the central Arctic (Shupe et al., 2022).

In situ data on the vertical distribution of aerosols are rare compared to data collected at ground level. In the last two decades, aircraft campaigns have allowed researchers to study the vertical distribution of aerosols, gaining insights into their transport, mixing, and interactions with clouds ~~(e.g. Yamanouchi et al., 2005; Brock et al., 2011; Willis et al., 2019; Wendisch et al., 2019; Jurányi et~~ (Yamanouchi et al., 2005; Brock et al., 2011; Willis et al., 2019; Wendisch et al., 2019; Jurányi et al., 2023; Wendisch et al., 2024). These fast-moving platforms can reach almost any remote location except the lowermost part of the atmosphere below 60-100 m above ground.

The Arctic atmospheric boundary layer (ABL) ~~is very~~ in winter is shallow, often less than 100 m deep, due to strong surface inversions and stable atmospheric conditions ~~(e.g. Vihma et al., 2014; Peng et al., 2023)~~(Vihma et al., 2014; Peng et al., 2023). Surface processes like water/ice/snow-atmosphere ~~exchange~~ exchanges of gases and aerosol particles have a significant impact on atmospheric composition in the Arctic ABL. Therefore, the lowest layer of the Arctic atmosphere exhibits unique dynamics, chemistry, and sensitivity to surface exchange that can only be resolved through in-situ measurements within this critical layer height. Arctic tethered balloon ~~(Ferrero et al., 2019; Cappelletti et al., 2022; Lata et al., 2023; Pohorsky et al., 2024)~~ (Ferrero et al., 2019; Cappelletti et al., 2022; Lata et al., 2023; Pilz et al., 2024; Pohorsky et al., 2024), and unmanned aerial vehicle (UAV) (Bates et al., 2013; de Boer et al., 2018) measurements can cover these lowest altitudes inaccessible ~~for~~ to aircraft, and provide high vertically resolved information on the occurring aerosol processes. However, these platforms can only be operated from specific locations with sufficient infrastructure available. Tethered balloons are fixed to a single point, whereas the operation range is very limited for a UAV. Towed bodies offer a possibility to perform long-ranged measurements either
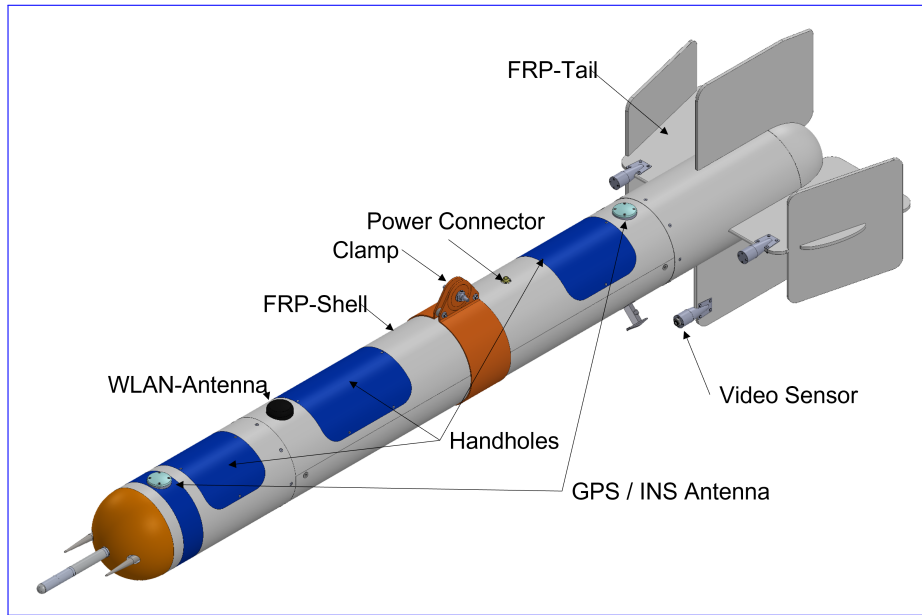
Figure 1. ~~CAD-drawing~~ Drawing of the T-Bird with main outer parts.

using a helicopter (Siebert et al., 2006; Pätzold et al., 2023) or an aircraft (Frey et al., 2009) to tow the instrument platform and eventually perform simultaneous measurements (aircraft and towed body) as well.

~~In order to be able to perform~~ To enable long-range turbulence and aerosol measurements in the lowermost layer of the polar atmosphere and simultaneously at a second altitude, the towed-body system, T-Bird, has been developed. Here, the

60   focus is on the technical description of the system (~~with special focus on~~ emphasizing the aerosol instrumentation) and ~~of its the~~ first application during the BACSAM (Boundary layer and Aerosol and Cloud Study in the Arctic, based on aircraft and T-Bird Measurements) campaign in the Arctic over the Fram Strait close to Svalbard. The technical description follows in ~~the next section and a first case study is described in~~ Section 2 and first acquired data are shown in Section 3. In a case study (Section 3.3.1~~. There~~), we focus on the question whether the vertical aerosol concentration profile follows the ABL structure

65   as obtained from potential temperature measurements.

2   The T-Bird–aircraft tandem measurement approach

2.1   Technical details of T-Bird

In this section we give a technical introduction to the T-Bird system. The T-Bird is a passive trailing body towed below the Alfred Wegener Institute's (AWI) ~~polar~~ aircraft Polar 5 or Polar 6. The body is attached to the aircraft by a cable of variable

70   length, which also supplies power from the aircraft to the ~~bird. It~~ trailing body. When the T-Bird is found in a winched-in position, it is mechanically fixed in the so-called nest, which is a frame construction located at the bottom of the aircraft
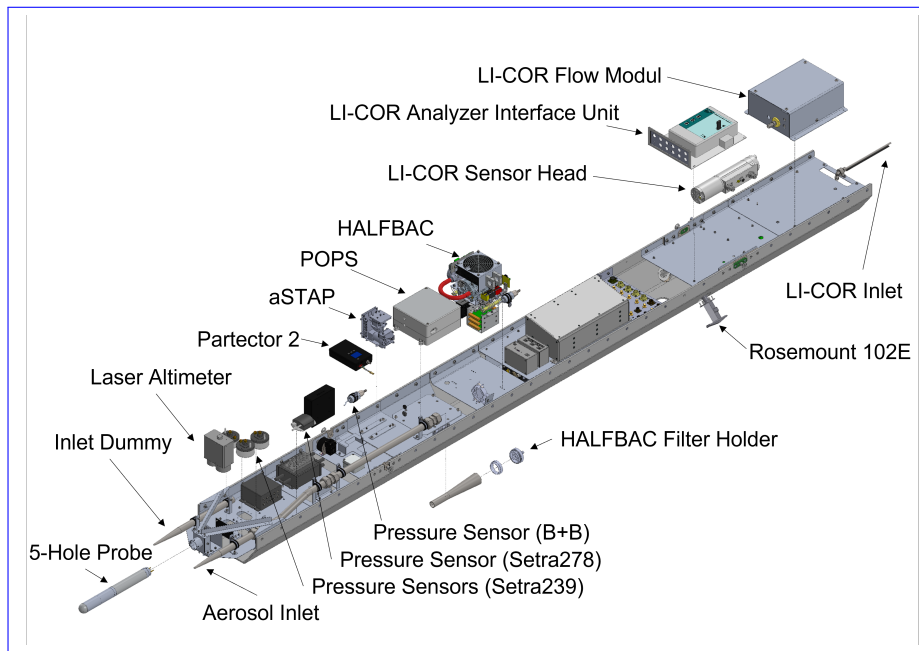
Figure 2. Exploding-view ~~CAD-drawing~~ drawing of the T-Bird system including descriptions of main sensors parts.

fuselage. The T-Bird can be winched to a maximum of ~100 m cable length allowing a vertical distance between ~~bird and plane~~ the trailing body and aircraft of about 60 m at typical measurement ~~speed~~ speeds of 185-220 km h^{-1}. The actual rules of the air safety regulation allows aircraft measurements higher than 60 m above ground~~, the use~~. The application of the T-Bird extends the measurement range to as low as ~10 m above flat surface. This unique measurement setup ~~allows us~~ enables to measure key parameters (e.g. meteorological, turbulence, and aerosol properties) within the Arctic ABL at the important 10 m level with a simultaneous second measurement level above realized by the sensors onboard the airplane. Beyond this, various other dual-level-measurements in polar regions are feasible~~, that are desirable for e.g. cloud and aerosol physics studies~~.

The overall design of the T-Bird's body, especially shape and size, is based on the successfully utilized EM-Bird (Haas et al., 2009). The outer body is made of fiber reinforced polymer (FRP)~~,~~; the inner structure consists of aluminium. The length of the T-Bird including nose boom and tail is 396 cm, with a diameter of 35 cm. The stabilising tail has a width and height of 107 cm. The fully equipped system weighs about 108 kg. Figure 1 shows a ~~CAD-drawing~~ drawing of the system. The T-Bird is anchored to the rope at a single clamp in the middle above its centre of gravity. The power connector is located behind the anchor clamp. Most data is sent in real time via wireless LAN to the data management system onboard the airplane. A video camera is located at the tail allowing real-time optical monitoring of the system environment during flight. Fully equipped, the installed instruments can be grouped into three payload types: aerosol, turbulence, and support equipment. Figure ~~1~~ 2 shows where the different sensors are situated in the T-Bird~~, in~~. In the following sections the different types of sensors will be introduced, with special focus on the aerosol instrumentation. The T-Bird's instrumental payload could also be adjusted, if required. However,

it should be kept in mind, that changing the T-Bird's configuration require a new certification, which has to be planned well in
90 advance and requires both, human and financial resources.

2.1.1 Turbulence instrumentation

The turbulence equipment is in principal the same as mounted on the aircraft where it has been used successfully in the polar
ABL during several campaigns (e.g. Ehrlich et al., 2019; Gryanik and Hartmann, 2022; Chechin et al., 2023). Namely, the
same five-hole probe (Aventech) is installed at the front of the T-Bird (Fig. 2)~~and provides~~, wherein Setra 239R and Setra
95 278 pressure transducers in combination with NI Compact Rio AD conversion modules provide static and dynamic (Pitot)
pressure and differential pressure measurements to derive the angles of attack and sideslip and finally the 3D wind vector with
a frequency of 100 Hz (Hartmann et al., 2018). A LI-COR infrared gas analyser (LI-COR Biosciences, LI-7200) measures
gas-phase H_2O and CO_2 concentrations through an actively aspirated and heated gas inlet situated at the back of the system.
The turbulence instrument bunch is completed by a Pt100 temperature sensor in a Rosemount housing (Rosemount, type 102E)
100 mounted at the underside of the T-Bird's rear third. The turbulence payload allows the determination of the momentum, sensible
and latent heat fluxes, and as will be shown in a later research paper(?), in combination with high frequency measurements of
aerosol particle concentrations, also particle fluxes.

2.1.2 Support instrumentation

Position, heading, and altitude information of the T-Bird is provided by a GPS (Global Positioning System) supported inertial
105 navigation system (INS, IMAR Navigation & Control iNAT-M200-SLN-DA) during flight. These are essential measurements
to correct the wind vector from the five-hole probe for the T-Bird's own movements. A camera system (AXIS F1005-E sensor
and AXIS F41 main unit) was installed with the camera sensor localized at the T-Bird's tail looking in flight direction to
document the overflown underground. Furthermore, a laser altimeter (ASTECH LDM 301) measures the height of the T-Bird
above ground.

2.1.3 Aerosol instrumentation

The T-Bird's aerosol inlet (Enviscope/Knebel, see Fig. 1) is mounted at the nose, next to the five-hole probe but behind it to
minimise its influence on turbulence measurements. In order to keep the T-Bird's symmetry and with that its balance, a blind
copy of the inlet was placed on the opposite side of the five-hole probe. The inlet is constructed of stainless steel, the ambient
air ~~first~~ enters a cone shaped diffuser (131.7 mm length, 3.7 mm opening diameter and 4 ° opening angle) to decelerate it.
115 This enables isokinetic sampling at a total flow of ~~3.2~~38.7 L min^{-1} and flight speed of $60\,\mathrm{m\,s^{-1}}$. The inlet enters the T-Bird
through a 22.1 mm diameter stainless steel tube, the individual sample lines to the various instruments were drawn from that
tube using angled inserts and connected to the individual instruments by conductive rubber tubing. Or, in case of the Partector 2
instrument, we applied PVC (Tygon) tubing, as recommended by the manufacturer (Asbach et al., 2016).

The amount of heat produced by the instruments during operation was high enough during the Arctic autumn test campaign

120 BACSAM ~~to keep them within their operational temperature range. The~~ (minimal measured outside temperature during flight of -21.4 °C) to keep the temperature high enough for the instruments installed inside the T-Bird to work properly. The temperature was not actively controlled, no extra heater nor cooler was installed in the T-Bird. The higher inside temperature of the T-Bird was also enough to keep the relative humidity of the aerosol sample below 40 %, no additional drying was used. An optional heating system can be installed for campaigns performed at even lower temperatures present.

125 Due to the limited space and payload capacity of the T-Bird, only miniaturized aerosol instruments ~~could be~~ were installed in it: a Partector 2, a portable optical particle spectrometer (POPS), a single channel tricolor absorption photometer (STAP), and a high-volume and light-weight balloon-borne filter sampler (HALFBAC). Table 1 shows a list of the T-Bird aerosol instrumentation, the measured properties and their time resolution. In the following we give a short introduction to the individual instruments.

130 A ~~partector~~Partector 2 (Naneos particle solutions GmbH, Windisch, Switzerland, from now on called Partector for simplicity) was installed in the T-Bird to measure the aerosol particle number concentration and the average diameter of particles in the diameter range of ∼10–300 nm. The instrument's measurement principle is based on unipolar corona diffusion charging and subsequent electrical current measurement. The unipolar charger is operated in a pulsed mode, which leads to packets of charged aerosol inducing currents in a two-stage Faraday Cage connected to high-sensitivity electrometers. Between the two

135 Faraday cages, an electrostatic precipitator is installed, where part of the charged aerosol particles are removed (Fierz et al., 2014). The measured two currents are dependent on the particles' size, and concentration. Using assumptions on the ~~form~~ shape of the particle number size distribution (~~having lognormal form~~ lognormal with a certain width and being monomodal), the two-stage measurement makes it possible to determine both, the total aerosol particle number ~~concentration~~ concentratio,n and an average aerosol particle diameter. The instrument's miniature size ($8.8 \times 14.2 \times 3.4$ cm), light weight (415 g), and the

140 lack of the need of a condensation fluid (butanol or water, that is needed by the most commonly used particle counters) makes it an ideal instrument to be operated in the T-Bird.

The POPS (Handix scientific, Fort Collins, CO,USA) is an optical particle counter and was developed for UAV and balloon deployment (Gao et al., 2016; Mei et al., 2020). Its small size and low power consumption makes it ideal for our applications. The instrument operates at a wavelength of 405 nm and optically sizes the sampled particles based on their single-particle

145 elastic light scattering ~~in the diameter~~ for diameters in the range approximately 140 nm to 3 µm. The POPS works with a sample-sheath flow system, where a single miniature pump is responsible for establishing both flows simultaneously. The pump draws air through the optical chamber from the instrument's aerosol inlet and the same time ambient air through an orifice and a particle filter as the sheath air. The sample flow rate through a laminar flow element is measured by a differential pressure sensor, and the pump speed is controlled such that the sample flow stays constant at $200\,\mathrm{cm^3\,min^{-1}}$. The particle free

150 sheath air ensures that the particles pass through the middle of the instruments laser beam. It is not monitored in the system, but the orifice (normally) guarantees its stable flow of $150\,\mathrm{cm^3\,min^{-1}}$.

The STAP (Brechtel Inc, Hayward, CA, USA – Model 9406) was built based on the Particle Soot Absorption Photometer (PSAP, Bond et al., 1999)~~instrument~~. Diffused light from three LED sources ~~centered around~~ with wavelengths of 445, 515, and

6

633 nm (blue, green, red) are alternatingly transmitted through two glass fiber filters, and the transmitted light is monitored by
photodetectors. One of the filters serves as a reference and no particles will be sampled through, the other will be loaded with
aerosol particles. Decrease in the transmitted light indicates the accumulation of absorbing particles on the filter, and provides a
measure of the light absorption coefficient at the three wavelengths~~are reported~~. These absorption coefficients can be converted
to equivalent BC (eBC, Petzold et al., 2013) mass concentrations. The instrument's lower detection limit is defined by its noise
level, which is $0.2\,\mathrm{Mm^{-1}}$ at $60\,\mathrm{s}$ averaging time (Bates et al., 2013). This translates to 10–$20\,\mathrm{ng\,m^{-3}}$ eBC dependent on the
applied mass absorption efficiency.

The filter sampler used for the collection of aerosol particles in the T-Bird is based on the TROPOS-built High-volume And
Light-weight Filter samplers for BAlloon-borne appliCation (HALFBAC, Grawe et al., 2023). It features a filter holder ($47\,\mathrm{mm}$,
in. inlet; PFA, Savillex, MN, USA) ~~;~~ a vacuum scroll pump (SVF-E0-50PF, Scroll Labs, USA)~~;~~, as well as temperature, pressure
before and behind the filter, volume and mass flow sensors. The instrument is controlled by means of a Raspberrry PI, which is
utilized for collecting the measured data and pump control. $800\,\mathrm{nm}$ pore size polycarboante filters (Nuclepore™ track-etched
membranes, Whatman, UK) were used, the sample flow rate was set to $30\,\mathrm{l\,min^{-1}}$, resulting in sampled air volumes per filter
between 2 and $7.2\,\mathrm{m^3}$.

2.2 Polar 6 aircraft and BACSAM aircraft campaign

Polar 6 is one of the research aircraft of Alfred Wegener Institute and was deployed to tow the T-Bird, and to host measurement
instrumentation onboard~~as well~~. The aircraft is a specifically modified Basler BT-67 aircraft for polar missions and has the
ability to fly at low cruising speeds of 185–$400\,\mathrm{km\,h^{-1}}$ performing measurements in an altitude range from 60 to $8000\,\mathrm{m}$
(Wesche et al., 2016).

The Boundary layer and Aerosol and Cloud Study in the Arctic, based on aircraft and T-Bird Measurements (BACSAM)
took place between 1 October 2022 and 16 October 2022 over the Fram Strait with an operation base of Longyearbyen airport
(78°14'43" N, 15°28'57" E) in Svalbard. The aircraft campaign was carried out within the framework of the project Arctic Am-
plification: Climate Relevant Atmospheric and Surface Processes and Feedback Mechanisms ~~((AC)³, Wendisch et al., 2023)~~
$(AC)^3$, (Wendisch et al., 2023).

The main goal of the campaign was to test the T-Bird for the first time in Arctic conditions, including dynamic flight
behaviour characterisation, T-Bird's instrumentation calibrations, testing and comparison, and ~~last but not least~~ performing
aerosol and turbulence measurements with both the T-Bird and the aircraft across the ABL up to the FT over open ocean and
over the marginal sea-ice zone. All together nine scientific flights were carried out with a total 29 hours of flight time.

2.3 Aircraft turbulence instrumentation

~~As already mentioned, the~~ The aircraft was equipped with a nose boom hosting the instrumentation bunch for turbulence
observations. This consist of a five-hole probe (Aventech) ~~and~~ with Setra 239R and Setra 278 pressure transducers, and Pt100
temperature sensor (Rosemount, type 102E). Additionally, there are a deiced (heated) Pt100-temperature sensor (Rosemount,
type 102E~~)~~, not used here for data analysis), and a humidity sensor (Vaisala HMT333) mounted on Polar 6 with dedicated

7

inlets. Furthermore, a LI-COR Biosciences, LI-7200 system for H_2O and CO_2 concentration measurements is installed in the aircraft cabine with an inlet on the aircraft's roof.

2.4 Aircraft aerosol instrumentation

The aircraft aerosol inlet with an intake diameter of 0.35 cm is located ahead of the engines, all aircraft aerosol instruments sampled air through this shrouded stainless-steel inlet diffuser. At the typical cruising speeds of Polar 6, the inlet has a transmission efficiency close to unity in the particle diameter range of 20 nm to 1 µm (Leaitch et al., 2016). The relative humidity of the aerosol sample was always below 30 %, due to the higher cabin temperature compared to the ambient temperature, no additional measure was needed to dry the aerosol.

The Polar 6 aerosol instrumentation, installed in the aircraft cabin during BACSAM consisted of a single particle soot photometer (SP2), a scanning mobility particle sizer (SMPS), and a high-volume flow aerosol particle filter sampler (HERA).

The SP2 (Droplet Measurement Technologies, Longmont, CO, USA) measures BC mass of individual aerosol particles in the mass equivalent diameter range from ∼80 nm to ∼600 nm (assuming void-free bulk material density of 1.8 g cm^{-3}, Moteki and Kondo, 2010). The BC detection is based on laser-induced incandescence, whereby a continuous-wave, high-intensity, intra-cavity laser (Nd: YAG crystal, wavelength of 1060 nm) heats up absorbing particles until they reach their vaporization temperature and emit incandescent light. Its intensity is proportional to the BC mass of the particle (Schwarz et al., 2006; Moteki and Kondo, 2010). The SP2 was calibrated before and after the measurement campaign using size selected fullerene particles (Moteki and Kondo, 2010; Gysel et al., 2011; Laborde et al., 2012). The calibration curves before and after the campaign agreed within 5 %, and therefore we can assume that the instrument's sensitivity remained constant during the campaign.

The SMPS (Wiedensohler et al., 2012) is a custom-built system, which consists of a differential mobility analyser (Vienna-type, custom built) and a condensational particle counter (TSI CPC3760A; TSI Incorporated, USA). It measures the aerosol number size distribution within the particle mobility diameter range of 10–850 nm. It was operated with a sheath flow of 5 l min^{-1} and sample flow of 1 l min^{-1}. A single SMPS scan lasted 300 s.

For the sampling of aerosol particles for subsequent offline analysis, concerning INP abundance and properties, the TROPOS-developed HERA sampler was used. HERA is an aerosol filter sampler for airbone-applications which has been described in detail in Grawe et al. (2023). It features a revolver-like arranged set of six filter holders, through which the sample flow is guided by a ball valve. During the T-Bird test campaign, the volumetric sample flow rate of HERA was set to 30 l min^{-1}. As filters, 800 nm pore-size polycarbonate filters (Nuclepore™ track-etched membranes, Whatman, UK) were used. The sampling time varied between 16 and 1666 min, resulting in sampled air-volumes between 0.4 and 4.5 m^3.

Platform		Instrument	Measured property	Size Range	Time resolution
Polar 6	Aerosol	SMPS	Number size distribution	10–850 nm	300 s
		SP2	BC mass concentration, size distribution	80–600 nm	1 Hz
		HERA	Filter Sampling	-	6 filters per flight
Polar 6	Turbulence	5-hole probe (Setra 239R and 278)	3-d wind components	-	100 Hz
		gas analyzer	CO_2/H_2O concentration	-	20 Hz
		Pt100	total air temperature	-	100 Hz
T-Bird	Aerosol	Partector	Number concentration, average diameter	10–300 nm	1 Hz
		POPS	Number size distribution	140–3300 nm	1 Hz
		~~a~~STAP	BC absorption coefficient	total	0.5 Hz
		HALFBAC	Filter Sampling	-	1 filter per flight
T-Bird	Turbulence	5-hole probe (Setra 239R and 278)	3-d wind components	-	100 Hz
		gas analyzer	CO_2/H_2O concentration	-	20 Hz
		Pt100	total air temperature	-	100 Hz
T-Bird	Support	INS	3d angles	-	100 Hz
		altimeter	height (~~agl~~ above ground level)	-	100 Hz
		camera	color images	-	50 Hz

Table 1. List of the scientific instrumentation including the measurement platform, the description of the measured quantity, size range and time resolution.

3 Results

3.1 T-Bird's flight behaviour

To ~~make a statement about~~ evaluate the flight characteristics of the T-Bird, a special flight test was carried out during the
220 BACSAM campaign. ~~In this test flight, a series of previously~~ A series of defined manoeuvres were flown to provide information on the interactions between the T-Bird and the towing aircraft. The manoeuvres were based on the explanations of Jategaonkar (2006) and were used to analyse the longitudinal and lateral motions of the T-Bird. Using INS and GPS data, a state space model was created. This revealed excellent flight characteristics of the T-Bird. Therefore, the T-Bird is characterised by uncritical flight behaviour with good damping behaviour in lateral motion, which makes it ideal for the scientific mission. ~~More detailed~~
225 ~~investigation could be made in further flight tests and through force measurements at certain angles of attack using wind tunnel tests.~~

9

T-Bird's motion relative to the towing plane represents a pendulum movement with a period depending on the length of rope. The largest amplitude of this movement is parallel to the flight direction and is a result of towing force changes due to vertical movement of the plane. This movement shows in speed ondulations of the bird. It has a negligible effect on the accuracy of the wind measurement as this movement is very precisely measured by the inertial system. Pendulum movement across flight direction results from turns of the aircraft to align on a desired track. The across movement eases out after two or three pendulum periods if the aircraft is flying steady on a straight track. The aerodynamics of the bird lead to very low sideslip angles, typically less than one degree during straight measurement flights. Even in regular turns sideslip angles greater than 2 or 3 degrees are very rarely exceeded. Thus the 5-hole-probe is nearly always in its specified and calibrated range.

3.2 Instrument performance in the T-Bird and in the aircraft

During BACSAM, most of the aerosol instrumentation functioned properly both in the aircraft and in the T-Bird as well, including the SMPS, HERA and SP2 in Polar 6 and Partector 2, HALFBAC in the T-Bird. We have encountered some issues with the POPS, as described below, however this problem will have been solved in future applications (?).

The aSTAP STAP showed no indication of malfunctioning, however during the BACSAM aircraft campaign we encountered extremely low BC concentrations below $1\,\mathrm{ng\,m^{-3}}$. This concentration is even much lower than the Arctic average summer season (out of Arctic haze season) concentration of $4.7\,\mathrm{ng\,m^{-3}}$ (Jurányi et al., 2023), and with that, the BC concentration was well below the detection limit of the instrument. The only times when the instrument delivered values above the noise level was directly before take off and after landing, when the aircraft emissions were sampled. With that, during BACSAM we only could test that the instrument is functional and that the data acquisition works properly. During future deployments, in spring season and/or closer to local sources we expect much higher BC concentrations above the instrument's detection limit, and with that valid measurements.

The POPS encountered flow problems during BACSAM. The instrument works with a sample-sheath flow system, where the particle-free sheath flow ensures that the aerosol particles pass through the middle of the laser beam. With the ram pressure present at the instrument's inlet during flight, the sample flow was always higher than the desired $200\,\mathrm{cm^3 min^{-1}}$. As a consequence, the instrument's pump was regulated down completely, the sheath flow was below the desired value, or even reversed. Additionally, the sample flow was as high that it could not be measured anymore (higher than the highest value that the laminar flow element could detect). After realizing this problem, as a fast solution, the inlet tube of the instrument was perforated such that the ram pressure induced excess flow was diverted before entering the instrument. This makeshift solution did not completely solve the problem, but at least the sample flow remained in the measurable range during the slower flight sections when the T-Bird was winched out. In following campaigns this problem has been avoided by placing a bypass tubing between the inlet and outlet of POPS.

The filter sampling instruments HALFBAC and HERA worked properly during the BACSAM campaing, 8 Filter samples with HERA and 18 with HALFBAC could be collected for INP analysis. The filter analysis is still in progress, a comparison between HALFBAC and HERA collected filter results will be subject of a separate future publication.

The main goal of the T-Bird application during future campaigns will be to obtain the vertical aerosol distribution in the entire ABL focusing on its lowest layers down to $10\,\text{m}$ above the surface. This will be done with simultaneous measurements at two altitudes such that highly resolved vertical profiles can be obtained with only few horizontal flight sections in different heights. Such missions involving flights with the T-Bird at the lowest possible altitude above ground were not within the scope of the first test campaign, the flight behaviour of the system was rather tested at safer, higher altitudes. Therefore, most of the time during the scientific flights, it can be expected, that both aircraft and T-Bird sampled aerosols from the same atmospheric layer with only negligible vertical gradients of aerosol properties. This gives us the opportunity to investigate the performance of the „miniature" aerosol instrumentation deployed in the T-Bird, by comparing their measured quantities to the „standard" instruments onboard of the Polar 6 aircraft. Though, we still have to keep in mind the above described instrumental problems.

3.2.1 Comparison of Partector and SMPS Results

The aerosol number concentration data from the ~~partector~~ Partector instrument deployed in the T-Bird was compared to the number concentration derived from the aircraft's SMPS measurements. All concentration data in this ~~manuscript~~ paper is reported as ambient concentration and is not corrected to standard conditions. For this comparison, all flight data was considered excluding solely take-off and landing. The data was separated according to the position of the T-Bird compared to the aircraft: i.e., we distinguish data when the T-Bird was in the nest directly below Polar 6 or when it was winched out completely ($\sim$60 m altitude difference between T-Bird and aircraft). With the T-Bird in the nest, the inlets of both systems are only separated by some meters and with that, sample almost the same air. For this situation we expect both instruments' delivered aerosol number concentration values to agree~~to a great extent~~, and the arising differences give us information on the instrumental and measurement uncertainties. For the case with winched out T-Bird, some additional uncertainty might originate from sampling different aerosol, but as it was mentioned before, due to the chosen flight patterns, we expect that only a small fraction of measurements are taken in layers with strong vertical gradients of aerosol properties. ~~Anyhow, the~~ The winched out T-Bird case was treated separately to check the extent of such an influence.

The measured SMPS aerosol number size distributions were integrated in the diameter range of 10–300 nm in order to match the size range of the ~~partector~~Partector. The 1-second data from the ~~partector~~ Partector was averaged to the 5-minute scan interval of the SMPS. Here, we have to take into account, that the SMPS counts the aerosol particles within a certain narrow diameter interval and scans through the considered diameter range. Therefore, when the aerosol concentration highly fluctuates within the scan time of the SMPS, the derived aerosol number concentration will be erroneous. ~~Thus, such~~ Such cases were sorted out after a manual inspection of each individual SMPS up- and down-scans.

The comparison of the aerosol number concentration between the ~~partector~~ Partector (N_{p}) and the SMPS (N_{10-300}) is shown in Figure 3 for both cases of winched in (green round markers) and winched out (red triangles) T-Bird. First of all, it is obvious that ~~partector~~ Partector data and SMPS data agree well with each other independent on the case confirming the assumption that most of the time we sampled the same aerosol. The only difference between the winched-in and winched-out case is the smaller concentration range of data for the latter case. The reason is that the T-Bird was only winched out during flying closer
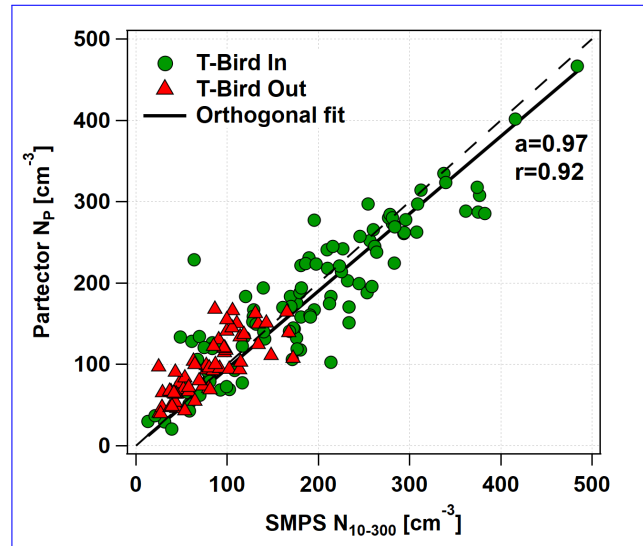
Figure 3. Comparison of the measured aerosol number concentration between the ~~partector 2~~ Partector and the SMPS between 10 and 300 nm particle diameter during the BACSAM campaign. The green round markers represent the periods when the T-Bird was directly below the aircraft, the red triangles when the T-Bird was winched out. The black solid line is the corresponding orthogonal regression line, the black dashed line shows the line of equality to guide the eyes.

to the surface (below $\sim$1000 m altitude), whereas transit flights (with T-Bird in its nest) took place at higher altitudes (between 2000-3000 m), where significantly higher concentrations were encountered during BACSAM.

295   Based on this result, we have chosen to investigate the relationship between the measured number concentration from the two different instruments without splitting the data according to the T-Bird's position. The orthogonal distance regression line (green line) forced through the origin shows that on average the Partector reported an N_p close to the SMPS with a slope of 0.97, and the data is highly correlated (correlation coefficient of 0.92). Despite the very good agreement, some individual measurement points can still show high scatter. It also has to be mentioned~~here~~, that due to the working principle of the

300 ~~partector~~ Partector, the original 1-second time resolution data (with a 4-second integration time~~setting) shows very~~) shows high noise at such low concentrations. The average ratio between N_p's standard deviation and mean value was 1.09 which means that the level of noise is comparable to the level of the measured signal. This should be considered for the further data analysis.

The average aerosol particle diameter obtained by the ~~partector can also be~~ Partector is compared to the measurements

305 of the SMPS~~, and for this comparison~~. For this comparison, the geometric mean diameter of the size distribution was chosen considering the diameter range between 10 and 300 nm. Even with perfect instrument performance, we do not expect an agreement between these values, since the „average diameter" reported by the ~~partector~~ Partector is based on many assumptions as mentioned in section 2.1.3. Only if the measured number size distribution exactly fulfilled all these assumptions, the ~~partector~~ Partector's average diameter would agree with the geometric mean diameter of the number size distribution. The
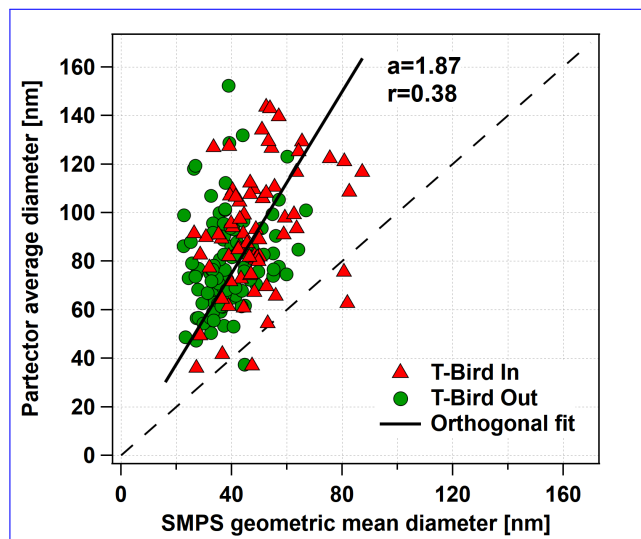
Figure 4. Comparison of the reported average diameter by the Partector ~~2~~ to the number mean diameter from the SMPS. The green round markers represent the periods when the T-Bird was directly below the aircraft, the red triangles when the T-Bird was winched out. The black solid line is the corresponding orthogonal regression line, the black dashed line shows the line of equality to guide the eye.

310   ~~partector~~ Partector data was again averaged through the duration of the single SMPS scans, and the same criterion for not considering the points with too highly fluctuating aerosol concentration was applied as before. The comparison is presented in Figure 4, showing the cases according to the T-Birds position separately (green round markers vs. red triangles).

      The ~~partector~~ Partector reports on average almost a factor ~~2~~ of two (orthogonal regression fit line has a slope of ~~1.98~~1.87) higher diameter than the geometric mean diameter measured by the SMPS, with a correlation coefficient of ~~0.42~~0.38. The

315   spread of the individual measurement points is high, but no difference between the two cases regarding the T-Bird's position can be identified. Based on this, we can conclude that the average diameter from the ~~partector~~ Partector cannot be directly compared to the geometric mean diameter of the number size distribution. Nevertheless, results might still be used as an indicator of the average size of the ultrafine particle size range.

3.2.2   Comparison of POPS and SMPS Results

320   The data originating from the POPS in the T-Bird was compared to the Polar 6's SMPS system. The instruments have a sufficient overlap within their size ranges (SMPS: 10–850 nm, POPS: 153–3000 nm) from 153 to 850 nm. To elucidate the effects of the above described flow problems of the POPS, we carried out a comparison of the SMPS and POPS measured size distributions. ~~Thereto, the~~ The data was sorted according to sample flow being within the instruments measurement range (flow in range) or being even higher (flow out of range). The number size distributions were integrated between 153 and 850 nm for both

325   instruments and the 1-second POPS data was averaged for the duration of the SMPS scan. SMPS scans were again excluded from the comparison, for which the POPS concentration fluctuated too much within the time period of one SMPS scan.
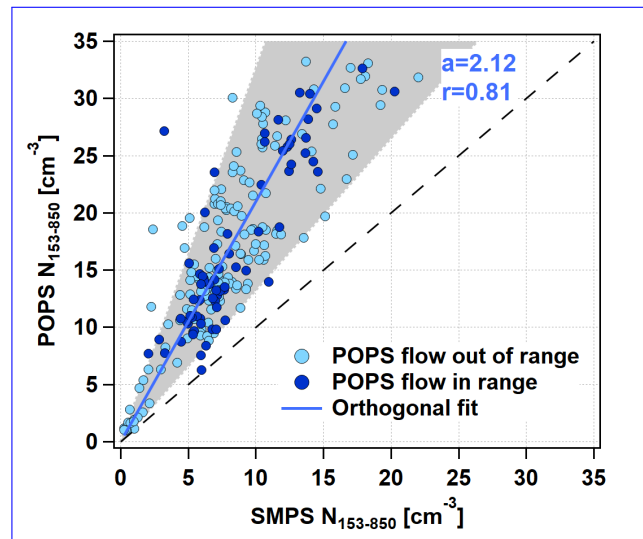
Figure 5. Comparison of the measured aerosol number concentration between the POPS instrument and the SMPS between 153 and 850 nm particle diameter during the BACSAM campaign. The dark blue markers represent the periods when the POPS sample flow was in the measurement range, the light blue markers the ones when the flow was even higher. The blue line is the corresponding orthogonal regression line, the black dashed line shows the line of equality to guide the eye. The light grey shaded area ends at the 95th and 5th percentiles of the ratio between the POPS and SMPS concentrations.

The comparison of the number concentration is shown in Figure 5~~: dark blue markers correspond to periods with a measurable sample flow, the light blue markers show the observations when the sample flow exceeded the maximum range of values that can be measured by the instrument~~. Firstly, there is no significant difference between the ~~two cases, secondly~~cases, if the POPS

330 sample flow was in the measureable range or not. Secondly, the POPS number concentration is highly correlated (correlation coefficient of 0.81) to the measured SMPS number concentration. However, due to the flow problem, it seems that the POPS on average counted ~~~2~~ two times higher concentration than the SMPS (slope of the orthogonal fit is 2.12). 90% of the points can be found within 1.22 and 3.26 times the number concentration of the SMPS ~~. This area is shown as a~~ (grey shading in Figure 5). This factor of 2.12 can be considered as the „counting efficiency" of the instrument.

335 To ~~be able to~~ investigate solely the sizing performance of the instrument, the POPS number size distributions were corrected with the previously determined „counting efficiency" factor. The median number size distributions after this correction are presented in Figure 6 ~~a~~ for the case when the ~~POPS~~ sample flow was ~~out of~~ within the measurement range ~~, and in Figure 6b for the case when the sample flow could be measured. For both flow cases the~~. The median number size distributions are not too far from each other and the ranges between 25th and 75th percentiles well overlap. Generally, the POPS seems to overestimate

340 the number of the „smaller" (<250 nm) particles and underestimate the number of the „larger" (>250 nm) particles. The case with the flow being outside of the measurement range shows very similar results (not shown here). This difference can partly exist because we compare different types of number size distributions with each other. The SMPS measures the number size distribution based on the mobility diameter whereas the POPS measures based on the optical diameter using Polystyrene Latex

14

particles with a refractive index of $1.615 + 0.001i$ (Gao et al., 2016) for calibration. ~~However, we expect that this effect is~~ ~~negligible compared to the sizing uncertainty caused by the mis-adjusted sheath flow. The too low , completely missing or even~~ ~~reversed sheath flow~~ As atmospheric aerosol particles may feature an in our case unknown size dependent refractive index, a direct qualitative comparison of POPS and SPMS measured size distributions is difficult. Another issue in this context is the too low sheath air flow inside POPS, which has the consequence that aerosol particles that were supposed to pass through the middle of the laser beam might have passed the laser closer to the edge of the beam with significantly lower intensity, and therefore falsely identified as smaller particles. In the measured number size distribution, this would appear as measuring too many smaller particles and too few larger ones, just ~~like we have observed in our case.~~

~~As the measured number concentration highly correlates to the number concentration of the SMPS, we will still~~ as our comparison shows. A similar effect can be caused by the presence of size dependent refractive index, if the larger aerosol particles have a significantly lower refractive index than the calibration aerosol. Due to all these uncertainties, in the following we will solely use the POPS data ~~in the following~~ as an indicator for the ~~number concentration~~ presence of larger (>153 nm) particles, which is justified due to the good correlation between the POPS's and SMPS's measured number concentration.
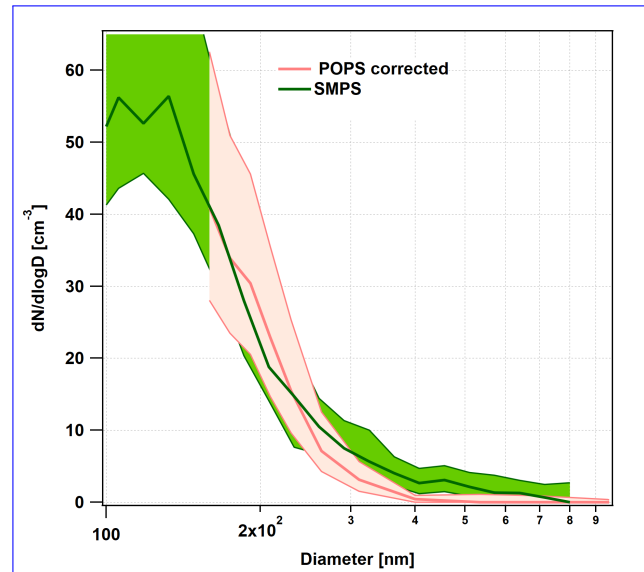

Figure 6. Comparison of the median number size distributions in the size range of 100 to 900 nm between POPS (~~red~~ rosa line, corrected to match the SMPS number concentration) and SMPS (green line) for the periods when the POPS sample flow was ~~out of the measurement range (a) and when it was~~ within the measurement range ~~(b)~~. The shadings were drawn between the 25th and 75th percentiles.

3.3 Case Study

In the following, we will focus on one ~~flight mission~~ research flight as an example to show the influence of mixing processes in the lower atmosphere (here below 2500 m) on the vertical distribution of aerosol particles. This flight took place on 05 October

360 2022 with the following flight pattern: after take-off, Polar 6 flew to the target area, followed by horizontal flight sections at increasing altitudes between two waypoints (WP1 and WP2). After that, the aircraft returned to the airbase and landed (Fig. 7).
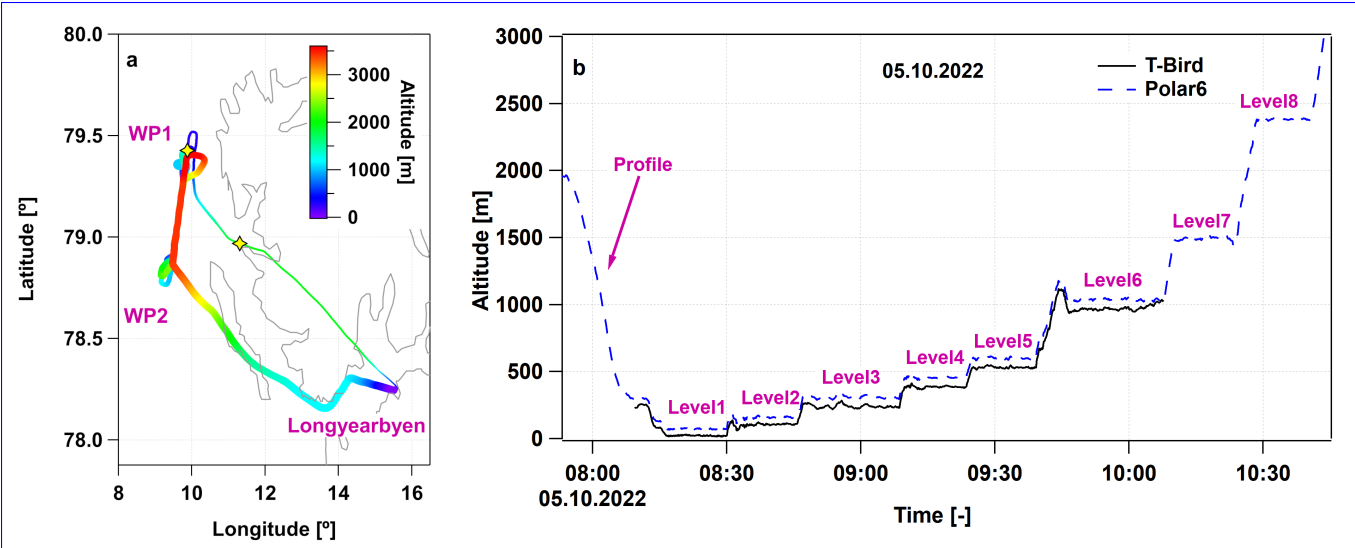
3.3.1 Research flight on the ~~05.10.2022~~05 October 2022

Figure 7. ~~Flight~~ Panel a: flight pattern on the 05 October 2022, the different colors indicate the flight level of the aircraft, the thickness of the pattern increases with the elapsed time. The yellow stars show the start and end points of the profile measurement. Panel b: flight altitude of the Polar 6 aircraft (blue dashed line) and the T-Bird (black solid line) as function of time on the 05 October 2022, measured by GPS. The T-Bird had only GPS reception when the system was winched out.

~~05 October 2022 was the date for the first scientific research flight.~~ Due to the pronounced lee effect caused by Svalbard's orography and prevailing easterly wind, a cloud-free area was formed west of Svalbard, which became the target area of
365 the ~~flight mission~~research flight. Within this area, a northern WP1 and a southern WP2 were defined (Fig. 7a), and between them, horizontal legs of approximately ~~10~~15 minutes duration (equivalent to about ~~65~~60 km distance) were performed at eight different altitudes (Fig. ~~??~~7b) above the open water surface. The length of the legs was chosen such, that independent of SMPS's exact scan start time, it was guaranteed, that two full scans could be performed at that single altitude. The T-Bird was winched out shortly before the first horizontal leg and was winched into its nest at the end of the sixth leg. Therefore, during the
370 measurements of the two legs with the highest altitudes, the T-Bird measured at the same altitude as the aircraft (Figure ~~??~~7b).
~~Flight altitude of the Polar 6 aircraft (blue dashed line) and the T-Bird (black solid line) as function of time on the 05 October 2022, measured by GPS. The T-Bird had only GPS reception when the system was winched out.~~ The T-bird also offers the possibility of measuring vertical profiles of meteorological properties such as temperature, pressure, wind components during climb and descent. POPS and Partector have a time resolution of 1Hz, however the Partector has a 4-32 s averaging
375 window, which is manually set dependent on the expected concentration. For the derivation of turbulence properties (e.g. fluxes,

turbulent kinetic energy) from high resolution wind and temperature measurements we need leg lengths at constant altitude of at least 8–10 km for statistical reasons.

Before reaching WP1 for the first time, the aircraft descended to the target area, and this provided us vertical profiles of meteorological quantities to investigate the structure of the lower atmosphere. Note that the descent started already close to the
380 western tip of Svalbard (Figure 7a, yellow star) and one should be aware of the fact that for this reason the potential temperature profile includes to some extent the effect of horizontal inhomogeneity along the distance flown during descent. ~~Namely, below 400, e.g.~~ Also between WP1 and WP2 the potential temperature changed ~~in the order of~~ by 1–2 K ~~between WP1 and WP2~~ along horizontal legs (not shown). Thus, ~~most accurately the~~ the mean stability in the lowermost layer can be analysed most accurately from leg averages ~~. These~~ rather than from the data obtained during descent at the northern end of the leg. These
385 horizontal leg averages are shown in Figure 8, whereas Figure 9 (grey solid line) shows the potential temperature as a function of the altitude during the descent to WP1.

The temperature profile at WP1 (Figure 9) reveals that the structure of the lower atmosphere is characterized by multiple inversions and mixed layers in between ~~starting with the near-surface ABL capped by a strong~~. The lowest one is the strong ABL capping inversion at about 100-130 m height. Above the inversion a ~~well mixed~~ well–mixed layer (in the following called
390 residual layer) follows again. And also this layer is capped by a strong inversion at about 750 m height, which reaches to about 1000 m. Then, another layer follows, which is also mixed but not so well as the residual layer. Finally, another inversion starts at about 1500 m height.

The leg averages show the potential temperature, wind speed (Figure 8 a, b), and turbulence quantities ~~,~~ (Figure 8 c, d), namely sensible heat flux and turbulent kinetic energy (TKE) ~~(Figure 8 c, d)~~. For the calculation of these turbulence quantities by the
395 eddy covariance method, the linear trends of wind and temperature between both ~~way points~~ WPs have been eliminated. Both the ~~profiles of~~ altitude dependent potential temperature and heat ~~flux~~ fluxes (both obtained from the horizontal flight legs, Figure 8 a, c) point to a weak convectively mixed ABL below about 100 ~~m~~ m height with small upward fluxes of sensible heat. It can be seen that the results from T-Bird (purple markers) ~~for potential temperature and wind showing a weak low-level jet, as well as fluxes of sensible heat and turbulent kinetic energy~~ and Polar 6 (green markers) fit very well to the results obtained from
400 Polar 6 (green markers). This ~~is remarkable, especially for the very small heat flux with values~~ concerns especially potential temperature and wind with a weak low level jet and turbulent kinetic energy. Also the sensible heat fluxes are reasonable but at 150 m, the heat flux seems to be overestimated by Polar 6 since negative values could be expected near the inversion bottom. However, one should not overinterpret the heat flux values, since they are close to the detection limit. ~~It shows a maximum near the surface and - as it should be in a convective ABL - decreasing values below the capping inversion to~~
405 ~~near zero in the inversion. Also~~ Usually, one would not expect an accuracy larger than ± 2 W m^{-2} because of further errors other than the sampling error (shown in the figure as error bars), which are calculated following Sreenivasan et al. (1978) and Fiedler et al. (2010). E.g., especially near the inversion bottom, inhomogeneity can occur along the leg as well as intermittent turbulence, which makes the measurements less reliable during such legs (see Tetzlaff et al., 2015). In such cases the measured flux profile can deviate from its ideal shape described, e.g. in Rampanelli and Zardi (2004). Nevertheless, it is impressing that
410 although the ABL is only slightly convective and heat fluxes are very small in this considered case, in this considered case,

17

the expected linear decrease from a maximum of heat flux near the surface to very small and sometimes negative (downward) values in the capping inversion is reproduced by the measurements. Also, the TKE altitude dependence with a maximum near the surface is physically reasonable~~for a shear driven ABL~~.
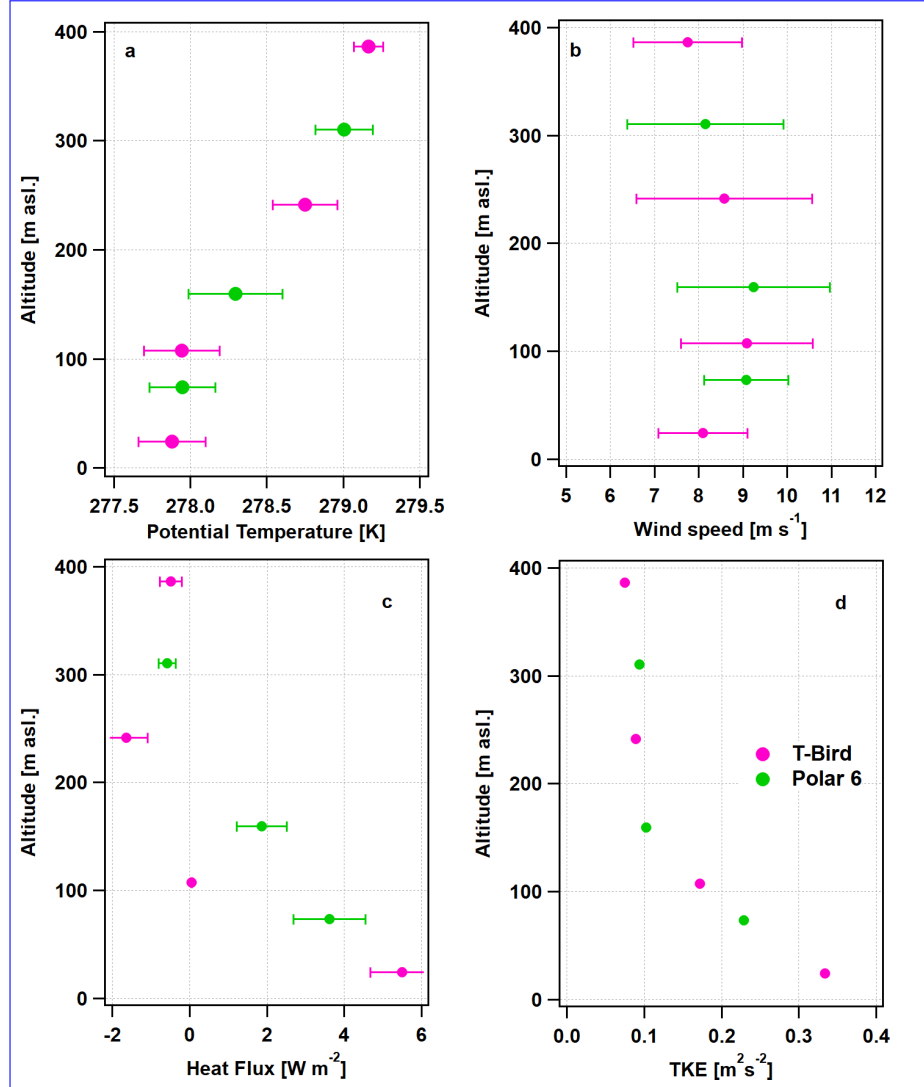

Figure 8. Turbulence measurements as function of altitude during the research flight on 05 October 2022 measured by Polar 6 (green markers) and the T-Bird (purple markers). Panel a shows the potential temperature (standard deviation as error bars), Panel b the wind speed (standard deviation as error bars), Panel c the sensible heat flux (sampling error as error bars) and Panel d the turbulent kinetic energy. The sampling error in Panel c at about 100 m is almost zero because it is proportional to the measured flux (Sreenivasan et al., 1978), which is close to zero at this point.
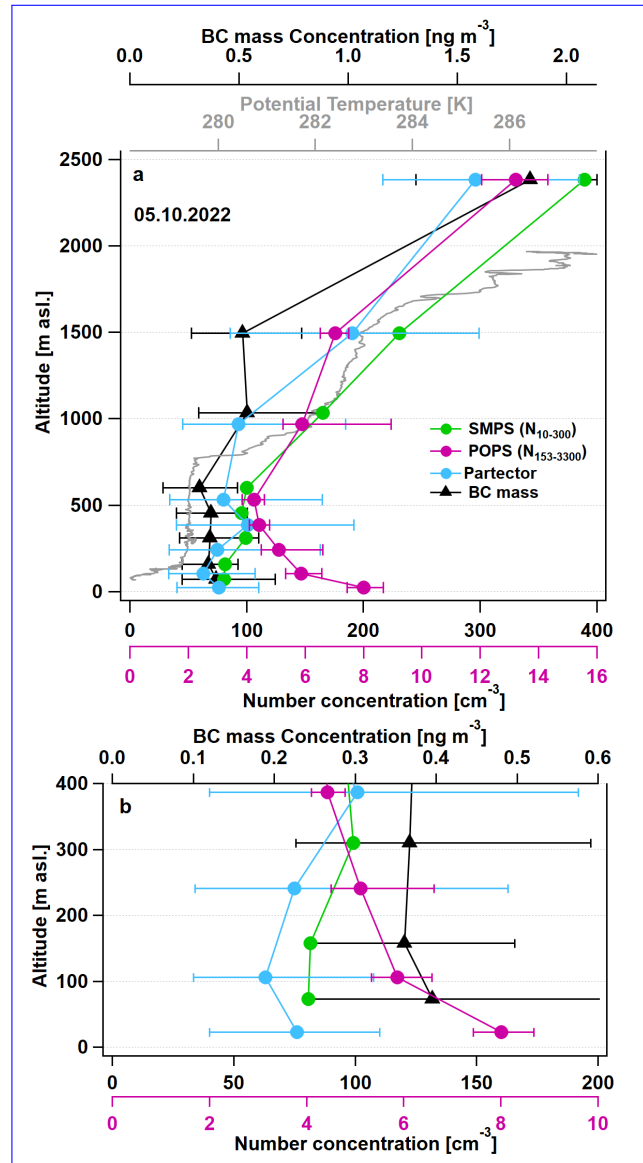
Figure 9. Aerosol properties as function of the altitude on 05 October 2022. The round markers show median aerosol number concentrations (blue: ~~partector 2~~ Partector, green: SMPS integrated between 10 and 300 nm and purple: POPS corrected number concentration, bottom purple x-axis), the black triangles (top black axis) show the median BC mass concentration whereas the solid grey line shows the potential temperature (top grey axis). The error bars show the 25th and 75th percentiles. Panel a shows the entire altitude range, whereas panel b shows the same data zoomed into the lowermost altitude range up to 400 m altitude for better visibility.

~~In order to~~ To investigate if and how the aerosol properties vary within these above mentioned different atmospheric layers,
415   median values and the 25th and 75th percentiles of the measured particle number concentrations encountered during each

horizontal leg were determined and are marked by horizontal whiskers in Figure 9. Since the SMPS instrument has a 5-minutes time resolution, during one altitude leg only 1-3 full scans could be performed. These scans were averaged and the number size distribution was integrated between 10 and 300 nm to obtain a number concentration comparable to the ~~partector~~Partector. The measured aerosol concentrations as a function of the measurement altitude are shown in Figure 9.
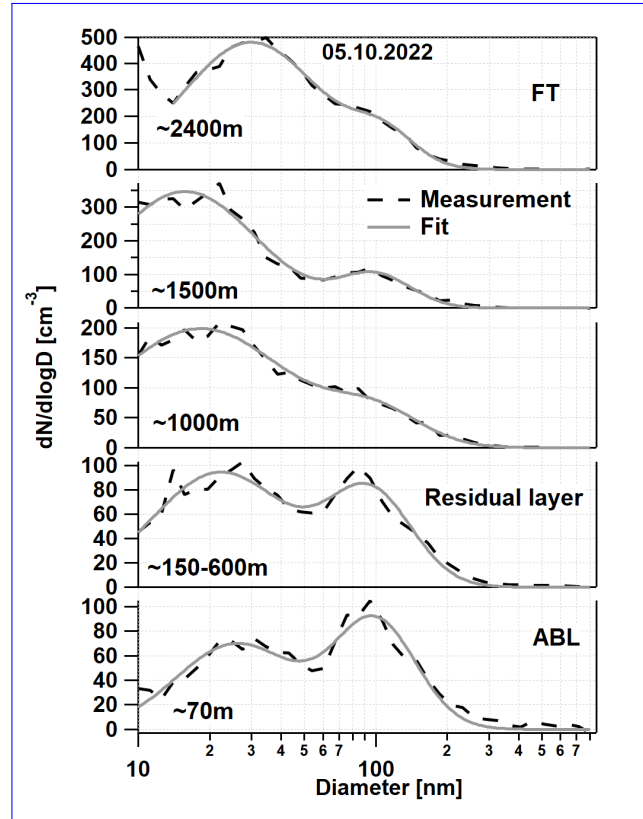

Figure 10. The averaged aerosol number size distribution at different atmospheric layers during the research flight on 05 October 2022. The black dashed lines show the measurement, the solid grey lines the fitted double lognormal distributions.

420   The median N_p measured by the ~~partector~~ Partector stays relative stable with increasing altitude through the boundary and residual layers ($\approx$20–550 m) with values between 63 and 101 cm^{-3}. Such low number concentrations are not unusual outside of the Arctic haze season in the region (e.g. Heintzenberg et al., 1991; Kupiszewski et al., 2013; Freud et al., 2017). Above the residual layer N_p increases with the altitude in the free troposphere (FT) reaching a median concentration of $\approx$300 cm^{-3} at 2400 m altitude. N_{10-300} measured by the SMPS features similar behaviour as N_p, with constant concentrations within the 425   boundary and residual layers with concentrations of 91–101 cm^{-3}, and increasing concentration within the FT and a highest value of 386 cm^{-3}. It is remarkable that the strong capping inversion above 100 m height has only little influence on the concentrations while there are changes in concentrations at the inversions in the higher layers.

The situation changes if the number concentration of larger particles is investigated. The median of the corrected POPS number concentration between 153 nm and 3 µm, is shown as purple dots in Figure 9 corresponding to the purple ~~x-axis~~abscissa.

Due to the instrumental problems, we take these values as ~~half-quantitative~~ qualitative measure for the amount of large particles. Thanks to the technology of the T-Bird, we were able to perform measurements as low as ≈ 20 m and this reveals a decreasing concentration from the ABL to the residual layer, which points to a source of large particles at the surface, which is probably sea-spray. Apart from this, the behaviour of the larger particles at higher altitudes follows the behaviour of the number concentration of the smaller particles. I.e., we find much higher concentrations in the FT than below with almost three times higher concentration at the highest measurement altitude, compared to the residual layer.

Table 2. Number size distribution fit parameters on the 05 October 2022 at the different altitude levels. N_1, N_2 are number concentrations, D_1 and D_2 are geometric mean diameters and σ_1 and σ_2 are geometric standard deviations of the first and second size distribution modes.

Altitude [m]	$N_1[\mathrm{cm}^{-3}]$	$D_1[\mathrm{nm}]$	σ_1 [-]	$N_2[\mathrm{cm}^{-3}]$	$D_2[\mathrm{nm}]$	σ_2 [-]
~70	44	25.9	1.79	38	99.7	1.48
~150–600	68	22.2	1.93	34	94.9	1.50
~1000	182	18.3	2.32	26	100.4	1.56
~1500	259	15.7	1.99	37	99.2	1.42
~2400	344	29.9	1.94	38	107.8	1.36

Additionally to the the number concentration, the SMPS aerosol number size distribution was also investigated at the different atmospheric layers (Fig. 10). The measured SMPS scans (1-3) were averaged within the individual layers and are shown as black dashed lines (please note the different y-axis for the different panels). To ~~be able to follow better~~ follow the change in the size distribution modes, a double lognormal function was fitted to the measured data and is shown as grey lines. The obtained fit parameters are shown in Table 2.

At the highest altitude, in the FT, we see a sudden increase of the particle number concentration at the lowest size bins (~10 nm), which can be an indication for new particle formation. However, we only see a small fraction of this mode due to the diameter limit of the SMPS. Therefore, we neither apply a fit to this mode nor speculate about it.

Furthermore, it seems that the increasing aerosol number concentration towards the FT is connected to the increasing number of particles below 40 nm. The concentration of the mode around 90–100 nm seems to stay relatively stable with concentrations between 25–40 cm^{-3}, whereas the concentration of the first mode around 15-30 nm particle size increases continuously from ~40 cm^{-3} in the ABL to more than 300 cm^{-3} in the FT.

The increased fraction of larger particles in the ABL can also be seen here, the number size distribution at diameters larger than the second mode does not converge to zero (better visible with logarithmic y-axis, not shown here), which might indicate the presence of another mode with even larger particle diameters around (400-600 nm). This points also to the presence of sea-spray over the open water emitting larger sea-salt particles into the ABL.

Last but not least, the behaviour of the measured BC mass concentration through the different atmospheric layers will be discussed (Figure 9, black dots with error bars showing the median and 25th and 75th percentiles), as measured by the SP2.

The median values ranged between $0.32\,\mathrm{ng\,m^{-3}}$ and $1.83\,\mathrm{ng\,m^{-3}}$. These values are extremely low compared to the median summer (outside of the Arctic haze season) BC concentration of $4.7\,\mathrm{ng\,m^{-3}}$ measured during 2 aircraft campaigns in the European and Canadian Arctic region (Jurányi et al., 2023). The BC mass concentration follows the same pattern as the total aerosol number concentration with higher values in the FT, and lower ones in the residual and boundary layers. This indicates that the BC is ~~internally mixed and that~~ not freshly emitted and there is no larger source in the lower atmosphere on Svalbard.

To summarize the overall situation during the case study on 05 October 2022, we have encountered much higher aerosol number and BC mass concentration in the FT than in the layers below. This shows us that the FT is an important aerosol source, and particles are mainly transported downwards to the lower atmospheric layers. The origin of these particles might be long-range transport and recent new particle formation. The observed increased BC mass is an indication for the former, the presence of the high concentration of small particles for the latter. Next to this, the higher concentration of larger particles close to the open water surface suggests the presence of an additional local aerosol source of sea-spray.

4 Conclusions

The T-Bird towed instrument platform represents a valuable tool for studying aerosol and turbulence properties in the challenging low-altitude regions of the polar atmosphere. Initial tests during the BACSAM campaign demonstrated the system's ability to capture key aerosol parameters, even in areas previously inaccessible to standard aircraft due to altitude constraints. Despite some technical challenges, the results indicate promising performance for future studies.

The comparison between the T-Bird's onboard aerosol instruments and the aircraft's standard instrumentation showed strong correlation in particle number concentration~~data~~, when sampling the same air-mass, confirming the functionality of the T-Bird system. Additionally, the ability to perform simultaneous two-level measurements offers new opportunities to study the vertical distribution of aerosols in relation to ~~, e.g.~~ turbulent ABL processes.

Future deployments of the T-Bird, especially under different seasonal and geographic conditions, will enhance its utility in providing critical data for understanding aerosol-cloud interactions, long-range transport of pollutants, and Arctic amplification~~processes~~. Continued refinement of the system, particularly in addressing instrumental limitations, will further improve its capabilities and reliability as a key resource for polar atmospheric research. To support better intercomparison and validation of observations, future measurement campaigns will also aim to integrate the T-Bird aerosol instrumentation into the aircraft itself, where feasible.

23

References

500 AMAP: Arctic Monitoring and Assessment Programme (AMAP), p. 148pp, 2021.

Asbach, C., Kaminski, H., Lamboy, Y., Schneiderwind, U., Fierz, M., and Todea, A. M.: Silicone sampling tubes can cause drastic artifacts in measurements with aerosol instrumentation based on unipolar diffusion charging, Aerosol Science and Technology, 50, 1375–1384, https://doi.org/10.1080/02786826.2016.1241858, 2016.

Barrie, L., Gregor, D., Hargrave, B., Lake, R., Muir, D., Shearer, R., Tracey, B., and Bidleman, T.: Arctic contaminants: sources, occurrence
505 and pathways, Sci. Total Environ., 122, 1–74, https://doi.org/https://doi.org/10.1016/0048-9697(92)90245-N, 1992.

Bates, T. S., Quinn, P. K., Johnson, J. E., Corless, A., Brechtel, F. J., Stalin, S. E., Meinig, C., and Burkhart, J. F.: Measurements of atmospheric aerosol vertical distributions above Svalbard, Norway, using unmanned aerial systems (UAS), Atmos. Meas. Tech., 6, 2115–2120, https://doi.org/10.5194/amt-6-2115-2013, 2013.

Bodhaine, B. A.: Barrow surface aerosol: 1976-1986, Atmos. Environ. (1967), 23, 2357–2369, https://doi.org/https://doi.org/10.1016/0004-
510 6981(89)90249-7, arctic Air Chemistry, 1989.

Bond, T. C., Anderson, T. L., and Campbell, D.: Calibration and Intercomparison of Filter-Based Measurements of Visible Light Absorption by Aerosols, Aerosol Science and Technology, 30, 582–600, https://doi.org/10.1080/027868299304435, 1999.

Brock, C. A., Cozic, J., Bahreini, R., Froyd, K. D., Middlebrook, A. M., McComiskey, A., Brioude, J., Cooper, O. R., Stohl, A., Aikin, K. C., de Gouw, J. A., Fahey, D. W., Ferrare, R. A., Gao, R.-S., Gore, W., Holloway, J. S., Hübler, G., Jefferson, A., Lack, D. A.,
515 Lance, S., Moore, R. H., Murphy, D. M., Nenes, A., Novelli, P. C., Nowak, J. B., Ogren, J. A., Peischl, J., Pierce, R. B., Pilewskie, P., Quinn, P. K., Ryerson, T. B., Schmidt, K. S., Schwarz, J. P., Sodemann, H., Spackman, J. R., Stark, H., Thomson, D. S., Thornberry, T., Veres, P., Watts, L. A., Warneke, C., and Wollny, A. G.: Characteristics, sources, and transport of aerosols measured in spring 2008 during the aerosol, radiation, and cloud processes affecting Arctic Climate (ARCPAC) Project, Atmos. Chem. Phys., 11, 2423–2453, https://doi.org/10.5194/acp-11-2423-2011, 2011.

520 Cappelletti, D., Petroselli, C., Mateos, D., Herreras, M., Ferrero, L., Losi, N., Gregori?, A., Frangipani, C., La Porta, G., Lonardi, M., Chernov, D., and Dekhtyareva, A.: Vertical profiles of black carbon and nanoparticles pollutants measured by a tethered balloon in Longyearbyen (Svalbard islands), Atmos. Environ., 290, 119 373, https://doi.org/https://doi.org/10.1016/j.atmosenv.2022.119373, 2022.

Chang, R. Y.-W., Leck, C., Graus, M., Müller, M., Paatero, J., Burkhart, J. F., Stohl, A., Orr, L. H., Hayden, K., Li, S.-M., Hansel, A., Tjernström, M., Leaitch, W. R., and Abbatt, J. P. D.: Aerosol composition and sources in the central Arctic Ocean during ASCOS, Atmos.
525 Chem. Phys., 11, 10 619–10 636, https://doi.org/10.5194/acp-11-10619-2011, 2011.

Chechin, D. G., Lüpkes, C., Hartmann, J., Ehrlich, A., and Wendisch, M.: Turbulent structure of the Arctic boundary layer in early summer driven by stability, wind shear and cloud-top radiative cooling: ACLOUD airborne observations, Atmospheric Chemistry and Physics, 23, 4685–4707, https://doi.org/10.5194/acp-23-4685-2023, 2023.

de Boer, G., Ivey, M., Schmid, B., Lawrence, D., Dexheimer, D., Mei, F., Hubbe, J., Bendure, A., Hardesty, J., Shupe, M. D., McComiskey,
530 A., Telg, H., Schmitt, C., Matrosov, S. Y., Brooks, I., Creamean, J., Solomon, A., Turner, D. D., Williams, C., Maahn, M., Argrow, B., Palo, S., Long, C. N., Gao, R.-S., and Mather, J.: A Bird's-Eye View: Development of an Operational ARM Unmanned Aerial Capability for Atmospheric Research in Arctic Alaska, B. Am. Meteorol. Soc., 99, 1197–1212, https://doi.org/https://doi.org/10.1175/BAMS-D-17-0156.1, 2018.

Ehrlich, A., Wendisch, M., Lüpkes, C., Buschmann, M., Bozem, H., Chechin, D., Clemen, H.-C., Dupuy, R., Eppers, O., Hartmann,
535 J., Herber, A., Jäkel, E., Järvinen, E., Jourdan, O., Kästner, U., Kliesch, L.-L., Köllner, F., Mech, M., Mertes, S., Neuber, R., Ruiz-

24

Donoso, E., Schnaiter, M., Schneider, J., Stapf, J., and Zanatta, M.: A comprehensive in situ and remote sensing data set from the Arctic CLoud Observations Using airborne measurements during polar Day (ACLOUD) campaign, Earth System Science Data, 11, 1853–1881, https://doi.org/10.5194/essd-11-1853-2019, 2019.

Ferrero, L., Ritter, C., Cappelletti, D., Moroni, B., Mo?nik, G., Mazzola, M., Lupi, A., Becagli, S., Traversi, R., Cataldi, M.,
540   Neuber, R., Vitale, V., and Bolzacchini, E.: Aerosol optical properties in the Arctic: The role of aerosol chemistry and dust composition in a closure experiment between Lidar and tethered balloon vertical profiles, Sci. Total Environ., 686, 452–467, https://doi.org/https://doi.org/10.1016/j.scitotenv.2019.05.399, 2019.

Fiedler, E., Lachlan-Cope, T., Renfrew, I., and King, J.: Convective heat transfer over thin ice covered coastal polynyas, Journal of Geophysical Research: Oceans, 115, 2010.

545   Fierz, M., Meier, D., Steigmeier, P., and Burtscher, H.: Aerosol Measurement by Induced Currents, Aerosol Science and Technology, 48, 350–357, https://doi.org/10.1080/02786826.2013.875981, 2014.

Freud, E., Krejci, R., Tunved, P., Leaitch, R., Nguyen, Q. T., Massling, A., Skov, H., and Barrie, L.: Pan-Arctic aerosol number size distributions: seasonality and transport patterns, Atmospheric Chemistry and Physics, 17, 8101–8128, https://doi.org/10.5194/acp-17-8101-2017, 2017.

550   Frey, W., Eichler, H., de Reus, M., Maser, R., Wendisch, M., and Borrmann, S.: A new airborne tandem platform for collocated measurements of microphysical cloud and radiation properties, Atmospheric Measurement Techniques, 2, 147–158, https://doi.org/10.5194/amt-2-147-2009, 2009.

Gao, R. S., Telg, H., McLaughlin, R. J., Ciciora, S. J., Watts, L. A., Richardson, M. S., Schwarz, J. P., Perring, A. E., Thornberry, T. D., Rollins, A. W., Markovic, M. Z., Bates, T. S., Johnson, J. E., and Fahey, D. W.: A light-weight, high-sensitivity particle spectrometer for
555   PM2.5 aerosol measurements, Aerosol Science and Technology, 50, 88–99, https://doi.org/10.1080/02786826.2015.1131809, 2016.

Grawe, S., Jentzsch, C., Schaefer, J., Wex, H., Mertes, S., and Stratmann, F.: Next-generation ice-nucleating particle sampling on board aircraft: characterization of the High-volume flow aERosol particle filter sAmpler (HERA), Atmospheric Measurement Techniques, 16, 4551–4570, https://doi.org/10.5194/amt-16-4551-2023, 2023.

Gryanik, V. M. and Hartmann, J.: On a Solution of the Closure Problem for Dry Convective Boundary Layer Turbulence and Beyond, Journal
560   of the Atmospheric Sciences, 79, 1405–1428, https://doi.org/10.1175/JAS-D-21-0107.1, 2022.

Gysel, M., Laborde, M., Olfert, J. S., Subramanian, R., and Gröhn, A. J.: Effective density of Aquadag and fullerene soot black carbon reference materials used for SP2 calibration, Atmos. Meas. Tech., 4, 2851–2858, https://doi.org/10.5194/amt-4-2851-2011, 2011.

Haas, C., Lobach, J., Hendricks, S., Rabenstein, L., and Pfaffling, A.: Helicopter-borne measurements of sea ice thickness, using a small and lightweight, digital EM system, J. Appl. Geophys., 67, 234–241, https://doi.org/https://doi.org/10.1016/j.jappgeo.2008.05.005, airborne
565   Geophysics, 2009.

Hartmann, J., Gehrmann, M., Kohnert, K., Metzger, S., and Sachs, T.: New calibration procedures for airborne turbulence measurements and accuracy of the methane fluxes during the AirMeth campaigns, Atmospheric Measurement Techniques, 11, 4567–4581, https://doi.org/10.5194/amt-11-4567-2018, 2018.

Heidam, N. Z., Wåhlin, P., and Christensen, J. H.: Tropospheric Gases and Aerosols in Northeast Greenland, J. Atmos. Sci., 56, 261 – 278,
570   https://doi.org/https://doi.org/10.1175/1520-0469(1999)056<0261:TGAAIN>2.0.CO;2, 1999.

Heintzenberg, J., Ström, J., Ogren, J., and Fimpel, H.-P.: Vertical profiles of aerosol properties in the summer troposphere of central Europe, scandinavia and the svalbard region, Atmospheric Environment. Part A. General Topics, 25, 621–627, https://doi.org/https://doi.org/10.1016/0960-1686(91)90059-G, 1991.

Jategaonkar, R. V.: Flight Vehicle System Identification: A Time-Domain Methodology, American Institute of Aeronautics and Astronautics, https://doi.org/10.2514/4.102790, 2006.

Jeffries, M. O., Overland, J. E., and Perovich, D. K.: The Arctic shifts to a new normal, Phys. Today, 66, 35–40, https://doi.org/10.1063/PT.3.2147, 2013.

Jurányi, Z., Zanatta, M., Lund, M. T., Samset, B. H., Skeie, R. B., Sharma, S., Wendisch, M., and Herber, A.: Atmospheric concentrations of black carbon are substantially higher in spring than summer in the Arctic., Commun. Earth Environ., 4, https://doi.org/https://doi.org/10.1038/s43247-023-00749-x, 2023.

Kupiszewski, P., Leck, C., Tjernström, M., Sjogren, S., Sedlar, J., Graus, M., Müller, M., Brooks, B., Swietlicki, E., Norris, S., and Hansel, A.: Vertical profiling of aerosol particles and trace gases over the central Arctic Ocean during summer, Atmospheric Chemistry and Physics, 13, 12 405–12 431, https://doi.org/10.5194/acp-13-12405-2013, 2013.

Laborde, M., Mertes, P., Zieger, P., Dommen, J., Baltensperger, U., and Gysel, M.: Sensitivity of the Single Particle Soot Photometer to different black carbon types, Atmos. Meas. Tech., 5, 1031–1043, https://doi.org/10.5194/amt-5-1031-2012, 2012.

Lata, N. N., Cheng, Z., Dexheimer, D., Zhang, D., Mei, F., and China, S.: Vertical Gradient of Size-Resolved Aerosol Compositions over the Arctic Reveals Cloud Processed Aerosol in-Cloud and above Cloud, Environ. Sci. Technol., 57, 5821–5830, https://doi.org/10.1021/acs.est.2c09498, pMID: 36971313, 2023.

Law, K. S., Roiger, A., Thomas, J. L., Marelle, L., Raut, J.-C., Dalsøren, S., Fuglestvedt, J., Tuccella, P., Weinzierl, B., and Schlager, H.: Local Arctic air pollution: Sources and impacts, Ambio, 46, 453–463, https://doi.org/10.1007/s13280-017-0962-2, 2017.

Leaitch, W. R., Korolev, A., Aliabadi, A. A., Burkart, J., Willis, M. D., Abbatt, J. P. D., Bozem, H., Hoor, P., Köllner, F., Schneider, J., Herber, A., Konrad, C., and Brauner, R.: Effects of 20–100 nm particles on liquid clouds in the clean summertime Arctic, Atmos. Chem. Phys., 16, 11 107–11 124, https://doi.org/10.5194/acp-16-11107-2016, 2016.

Mauritsen, T., Sedlar, J., Tjernström, M., Leck, C., Martin, M., Shupe, M., Sjogren, S., Sierau, B., Persson, P. O. G., Brooks, I. M., and Swietlicki, E.: An Arctic CCN-limited cloud-aerosol regime, Atmos. Chem. Phys., 11, 165–173, https://doi.org/10.5194/acp-11-165-2011, 2011.

Mei, F., McMeeking, G., Pekour, M., Gao, R.-S., Kulkarni, G., China, S., Telg, H., Dexheimer, D., Tomlinson, J., and Schmid, B.: Performance Assessment of Portable Optical Particle Spectrometer (POPS), SENSORS, 20, https://doi.org/10.3390/s20216294, 2020.

Moteki, N. and Kondo, Y.: Dependence of Laser-Induced Incandescence on Physical Properties of Black Carbon Aerosols: Measurements and Theoretical Interpretation, Aerosol Sci. Tech., 44, 663–675, https://doi.org/10.1080/02786826.2010.484450, 2010.

Nguyen, Q. T., Glasius, M., Sørensen, L. L., Jensen, B., Skov, H., Birmili, W., Wiedensohler, A., Kristensson, A., Nøjgaard, J. K., and Massling, A.: Seasonal variation of atmospheric particle number concentrations, new particle formation and atmospheric oxidation capacity at the high Arctic site Villum Research Station, Station Nord, Atmos. Chem. Phys., 16, 11 319–11 336, https://doi.org/10.5194/acp-16-11319-2016, 2016.

Pätzold, F., Bretschneider, L., Nowak, S., Brandt, B., Schlerf, A., Asmussen, M. O., Bollmann, S., Bärfuss, K., Harm-Altstädter, B., Hecker, P., et al.: HELiPOD—Revolution and evolution of a helicopter-borne measurement system for multidisciplinary research in demanding environments, Elementa: Science of the Anthropocene, 11, 2023.

Peng, S., Yang, Q., Shupe, M. D., Xi, X., Han, B., Chen, D., Dahlke, S., and Liu, C.: The characteristics of atmospheric boundary layer height over the Arctic Ocean during MOSAiC, Atmospheric Chemistry and Physics, 23, 8683–8703, https://doi.org/10.5194/acp-23-8683-2023, 2023.

Petzold, A., Ogren, J. A., Fiebig, M., Laj, P., Li, S.-M., Baltensperger, U., Holzer-Popp, T., Kinne, S., Pappalardo, G., Sugimoto, N., Wehrli, C., Wiedensohler, A., and Zhang, X.-Y.: Recommendations for reporting "black carbon" measurements, Atmos. Chem. Phys., 13, 8365–8379, https://doi.org/10.5194/acp-13-8365-2013, 2013.

Pilz, C., Cassano, J. J., de Boer, G., Kirbus, B., Lonardi, M., Pöhlker, M., Shupe, M. D., Siebert, H., Wendisch, M., and Wehner, B.: Tethered balloon measurements reveal enhanced aerosol occurrence aloft interacting with Arctic low-level clouds, Elementa: Science of the Anthropocene, 12, 00 120, https://doi.org/10.1525/elementa.2023.00120, 2024.

Pithan, F. and Mauritsen, T.: Arctic amplification dominated by temperature feedbacks in contemporary climate models, Nat. Geosci., 7, 181–184, https://doi.org/10.1038/ngeo2071, 2014.

Platt, S. M., Hov, Ø., Berg, T., Breivik, K., Eckhardt, S., Eleftheriadis, K., Evangeliou, N., Fiebig, M., Fisher, R., Hansen, G., Hansson, H.-C., Heintzenberg, J., Hermansen, O., Heslin-Rees, D., Holmén, K., Hudson, S., Kallenborn, R., Krejci, R., Krognes, T., Larssen, S., Lowry, D., Lund Myhre, C., Lunder, C., Nisbet, E., Nizzetto, P. B., Park, K.-T., Pedersen, C. A., Aspmo Pfaffhuber, K., Röckmann, T., Schmidbauer, N., Solberg, S., Stohl, A., Ström, J., Svendby, T., Tunved, P., Tørnkvist, K., van der Veen, C., Vratolis, S., Yoon, Y. J., Yttri, K. E., Zieger, P., Aas, W., and Tørseth, K.: Atmospheric composition in the European Arctic and 30 years of the Zeppelin Observatory, Ny-Ålesund, Atmos. Chem. Phys., 22, 3321–3369, https://doi.org/10.5194/acp-22-3321-2022, 2022.

Pohorsky, R., Baccarini, A., Tolu, J., Winkel, L. H. E., and Schmale, J.: Modular Multiplatform Compatible Air Measurement System (MoMuCAMS): a new modular platform for boundary layer aerosol and trace gas vertical measurements in extreme environments, Atmospheric Measurement Techniques, 17, 731–754, https://doi.org/10.5194/amt-17-731-2024, 2024.

Polissar, A., Hopke, P., Paatero, P., Kaufmann, Y., Hall, D., Bodhaine, B., Dutton, E., and Harris, J.: The aerosol at Barrow, Alaska: long-term trends and source locations, Atmos. Environ., 33, 2441–2458, https://doi.org/https://doi.org/10.1016/S1352-2310(98)00423-3, 1999.

Rampanelli, G. and Zardi, D.: A method to determine the capping inversion of the convective boundary layer, Journal of Applied Meteorology, 43, 925–933, 2004.

Schmale, J., Zieger, P., and Ekman, A. M. L.: Aerosols in current and future Arctic climate, Nat. Clim. Change, 11, 95–105, https://doi.org/10.1038/s41558-020-00969-5, 2021.

Schwarz, J. P., Gao, R. S., Fahey, D. W., Thomson, D. S., Watts, L. A., Wilson, J. C., Reeves, J. M., Darbeheshti, M., Baumgardner, D. G., Kok, G. L., Chung, S. H., Schulz, M., Hendricks, J., Lauer, A., Kärcher, B., Slowik, J. G., Rosenlof, K. H., Thompson, T. L., Langford, A. O., Loewenstein, M., and Aikin, K. C.: Single-particle measurements of midlatitude black carbon and light-scattering aerosols from the boundary layer to the lower stratosphere, J. Geophys. Res.-Atmos., 111, https://doi.org/https://doi.org/10.1029/2006JD007076, 2006.

Shupe, M. D., Rex, M., Blomquist, B., Persson, P. O. G., Schmale, J., Uttal, T., Althausen, D., Angot, H., Archer, S., Bariteau, L., Beck, I., Bilberry, J., Bucci, S., Buck, C., Boyer, M., Brasseur, Z., Brooks, I. M., Calmer, R., Cassano, J., Castro, V., Chu, D., Costa, D., Cox, C. J., Creamean, J., Crewell, S., Dahlke, S., Damm, E., de Boer, G., Deckelmann, H., Dethloff, K., Dütsch, M., Ebell, K., Ehrlich, A., Ellis, J., Engelmann, R., Fong, A. A., Frey, M. M., Gallagher, M. R., Ganzeveld, L., Gradinger, R., Graeser, J., Greenamyer, V., Griesche, H., Griffiths, S., Hamilton, J., Heinemann, G., Helmig, D., Herber, A., Heuzé, C., Hofer, J., Houchens, T., Howard, D., Inoue, J., Jacobi, H.-W., Jaiser, R., Jokinen, T., Jourdan, O., Jozef, G., King, W., Kirchgaessner, A., Klingebiel, M., Krassovski, M., Krumpen, T., Lampert, A., Landing, W., Laurila, T., Lawrence, D., Lonardi, M., Loose, B., Lüpkes, C., Maahn, M., Macke, A., Maslowski, W., Marsay, C., Maturilli, M., Mech, M., Morris, S., Moser, M., Nicolaus, M., Ortega, P., Osborn, J., Pätzold, F., Perovich, D. K., Petäjä, T., Pilz, C., Pirazzini, R., Posman, K., Powers, H., Pratt, K. A., Preußer, A., Quéléver, L., Radenz, M., Rabe, B., Rinke, A., Sachs, T., Schulz, A., Siebert, H., Silva, T., Solomon, A., Sommerfeld, A., Spreen, G., Stephens, M., Stohl, A., Svensson, G., Uin, J., Viegas, J., Voigt, C., von der Gathen, P.,

Wehner, B., Welker, J. M., Wendisch, M., Werner, M., Xie, Z., and Yue, F.: Overview of the MOSAiC expedition: Atmosphere, Elementa: Science of the Anthropocene, 10, 00 060, https://doi.org/10.1525/elementa.2021.00060, 2022.

650 Siebert, H., Franke, H., Lehmann, K., Maser, R., Saw, E. W., Schell, D., Shaw, R. A., and Wendisch, M.: Probing Finescale Dynamics and Microphysics of Clouds with Helicopter-Borne Measurements, Bulletin of the American Meteorological Society, 87, 1727 – 1738, https://doi.org/10.1175/BAMS-87-12-1727, 2006.

Sirois, A. and Barrie, L. A.: Arctic lower tropospheric aerosol trends and composition at Alert, Canada: 1980-1995, J. Geophys. Res-Atmos., 104, 11 599–11 618, https://doi.org/https://doi.org/10.1029/1999JD900077, 1999.

655 Sreenivasan, K., Chambers, A., and Antonia, R.: Accuracy of moments of velocity and scalar fluctuations in the atmospheric surface layer, Boundary-Layer Meteorology, 14, 341–359, 1978.

Szopa, S., Naik, V., Adhikary, B., Artaxo, P., Berntsen, T., Collins, W., Fuzzi, S., Gallardo, L., Kiendler-Scharr, A., Klimont, Z., Liao, H., Unger, N., and Zanis, P.: Short-Lived Climate Forcers, pp. 817–922, Cambridge University Press, Cambridge, United Kingdom and New York, NY, USA, https://doi.org/10.1017/9781009157896.008, 2021.

660 Tetzlaff, A., Lüpkes, C., and Hartmann, J.: Aircraft-based observations of atmospheric boundary-layer modification over Arctic leads, Quarterly Journal of the Royal Meteorological Society, 141, 2839–2856, 2015.

Tjernström, M., Leck, C., Birch, C. E., Bottenheim, J. W., Brooks, B. J., Brooks, I. M., Bäcklin, L., Chang, R. Y.-W., de Leeuw, G., Di Liberto, L., de la Rosa, S., Granath, E., Graus, M., Hansel, A., Heintzenberg, J., Held, A., Hind, A., Johnston, P., Knulst, J., Martin, M., Matrai, P. A., Mauritsen, T., Müller, M., Norris, S. J., Orellana, M. V., Orsini, D. A., Paatero, J., Persson, P. O. G., Gao, Q., Rauschenberg, C.,
665 Ristovski, Z., Sedlar, J., Shupe, M. D., Sierau, B., Sirevaag, A., Sjogren, S., Stetzer, O., Swietlicki, E., Szczodrak, M., Vaattovaara, P., Wahlberg, N., Westberg, M., and Wheeler, C. R.: The Arctic Summer Cloud Ocean Study (ASCOS): overview and experimental design, Atmospheric Chemistry and Physics, 14, 2823–2869, https://doi.org/10.5194/acp-14-2823-2014, 2014.

Vihma, T., Pirazzini, R., Fer, I., Renfrew, I. A., Sedlar, J., Tjernström, M., Lüpkes, C., Nygård, T., Notz, D., Weiss, J., Marsan, D., Cheng, B., Birnbaum, G., Gerland, S., Chechin, D., and Gascard, J. C.: Advances in understanding and parameterization of small-scale physical
670 processes in the marine Arctic climate system: a review, Atmospheric Chemistry and Physics, 14, 9403–9450, https://doi.org/10.5194/acp-14-9403-2014, 2014.

Wendisch, M., Brückner, M., Burrows, J. P., Crewell, S., Dethloff, K., Ebell, K., Lüpkes, C., Macke, A., Notholt, J., Quaas, J., Rinke, A., and I., T.: Understanding Causes and Effects of Rapid Warming in the Arctic, Arctic. Eos, 98, 22–26, https://doi.org/10.1029/2017EO064803, 2017.

675 Wendisch, M., Macke, A., Ehrlich, A., Lüpkes, C., Mech, M., Chechin, D., Dethloff, K., Velasco, C. B., Bozem, H., Brückner, M., Clemen, H.-C., Crewell, S., Donth, T., Dupuy, R., Ebell, K., Egerer, U., Engelmann, R., Engler, C., Eppers, O., Gehrmann, M., Gong, X., Gottschalk, M., Gourbeyre, C., Griesche, H., Hartmann, J., Hartmann, M., Heinold, B., Herber, A., Herrmann, H., Heygster, G., Hoor, P., Jafariserajehlou, S., Jäkel, E., Järvinen, E., Jourdan, O., Kästner, U., Kecorius, S., Knudsen, E. M., Köllner, F., Kretzschmar, J., Lelli, L., Leroy, D., Maturilli, M., Mei, L., Mertes, S., Mioche, G., Neuber, R., Nicolaus, M., Nomokonova, T., Notholt, J., Palm, M., van Pinx-
680 teren, M., Quaas, J., Richter, P., Ruiz-Donoso, E., Schäfer, M., Schmieder, K., Schnaiter, M., Schneider, J., Schwarzenböck, A., Seifert, P., Shupe, M. D., Siebert, H., Spreen, G., Stapf, J., Stratmann, F., Vogl, T., Welti, A., Wex, H., Wiedensohler, A., Zanatta, M., and Zeppenfeld, S.: The Arctic Cloud Puzzle: Using ACLOUD/PASCAL Multiplatform Observations to Unravel the Role of Clouds and Aerosol Particles in Arctic Amplification, B. Am. Meteorol. Soc., 100, 841–871, https://doi.org/10.1175/BAMS-D-18-0072.1, 2019.

Wendisch, M., Brückner, M., Crewell, S., Ehrlich, A., Notholt, J., Lüpkes, C., Macke, A., Burrows, J. P., Rinke, A., Quaas, J., Maturilli,
685 M., Schemann, V., Shupe, M. D., Akansu, E. F., Barrientos-Velasco, C., Bärfuss, K., Blechschmidt, A.-M., Block, K., Bougoudis, I.,

Bozem, H., Böckmann, C., Bracher, A., Bresson, H., Bretschneider, L., Buschmann, M., Chechin, D. G., Chylik, J., Dahlke, S., Deneke, H., Dethloff, K., Donth, T., Dorn, W., Dupuy, R., Ebell, K., Egerer, U., Engelmann, R., Eppers, O., Gerdes, R., Gierens, R., Gorodetskaya, I. V., Gottschalk, M., Griesche, H., Gryanik, V. M., Handorf, D., Harm-Altstädter, B., Hartmann, J., Hartmann, M., Heinold, B., Herber, A., Herrmann, H., Heygster, G., Höschel, I., Hofmann, Z., Hölemann, J., Hünerbein, A., Jafariserajehlou, S., Jäkel, E., Jacobi, C., Janout,

690   M., Jansen, F., Jourdan, O., Jurányi, Z., Kalesse-Los, H., Kanzow, T., Käthner, R., Kliesch, L. L., Klingebiel, M., Knudsen, E. M., Kovács, T., Körtke, W., Krampe, D., Kretzschmar, J., Kreyling, D., Kulla, B., Kunkel, D., Lampert, A., Lauer, M., Lelli, L., von Lerber, A., Linke, O., Löhnert, U., Lonardi, M., Losa, S. N., Losch, M., Maahn, M., Mech, M., Mei, L., Mertes, S., Metzner, E., Mewes, D., Michaelis, J., Mioche, G., Moser, M., Nakoudi, K., Neggers, R., Neuber, R., Nomokonova, T., Oelker, J., Papakonstantinou-Presvelou, I., Pätzold, F., Pefanis, V., Pohl, C., van Pinxteren, M., Radovan, A., Rhein, M., Rex, M., Richter, A., Risse, N., Ritter, C., Rostosky, P., Rozanov,

695   V. V., Donoso, E. R., Saavedra-Garfias, P., Salzmann, M., Schacht, J., Schäfer, M., Schneider, J., Schnierstein, N., Seifert, P., Seo, S., Siebert, H., Soppa, M. A., Spreen, G., Stachlewska, I. S., Stapf, J., Stratmann, F., Tegen, I., Viceto, C., Voigt, C., Vountas, M., Walbröl, A., Walter, M., Wehner, B., Wex, H., Willmes, S., Zanatta, M., and Zeppenfeld, S.: Atmospheric and Surface Processes, and Feedback Mechanisms Determining Arctic Amplification: A Review of First Results and Prospects of the (AC)3 Project, B. Am. Meteorol. Soc., 104, E208–E242, https://doi.org/10.1175/BAMS-D-21-0218.1, 2023.

700 Wendisch, M., Crewell, S., Ehrlich, A., Herber, A., Kirbus, B., Lüpkes, C., Mech, M., Abel, S. J., Akansu, E. F., Ament, F., Aubry, C., Becker, S., Borrmann, S., Bozem, H., Brückner, M., Clemen, H.-C., Dahlke, S., Dekoutsidis, G., Delanoë, J., De La Torre Castro, E., Dorff, H., Dupuy, R., Eppers, O., Ewald, F., George, G., Gorodetskaya, I. V., Grawe, S., Groß, S., Hartmann, J., Henning, S., Hirsch, L., Jäkel, E., Joppe, P., Jourdan, O., Jurányi, Z., Karalis, M., Kellermann, M., Klingebiel, M., Lonardi, M., Lucke, J., Luebke, A., Maahn, M., Maherndl, N., Maturilli, M., Mayer, B., Mayer, J., Mertes, S., Michaelis, J., Michalkov, M., Mioche, G., Moser, M., Müller, H., Neggers, R., Ori,

705   D., Paul, D., Paulus, F., Pilz, C., Pithan, F., Pöhlker, M., Pörtge, V., Ringel, M., Risse, N., Roberts, G. C., Rosenburg, S., Röttenbacher, J., Rückert, J., Schäfer, M., Schäfer, J., Schemannn, V., Schirmacher, I., Schmidt, J., Schmidt, S., Schneider, J., Schnitt, S., Schwarz, A., Siebert, H., Sodemann, H., Sperzel, T., Spreen, G., Stevens, B., Stratmann, F., Svensson, G., Tatzelt, C., Tuch, T., Vihma, T., Voigt, C., Volkmer, L., Walbröl, A., Weber, A., Wehner, B., Wetzel, B., Wirth, M., and Zinner, T.: Overview: Quasi-Lagrangian observations of Arctic air mass transformations – Introduction and initial results of the HALO-(AC)[3] aircraft campaign, Atmospheric Chemistry and

710   Physics, 24, 8865–8892, https://doi.org/10.5194/acp-24-8865-2024, 2024.

Wesche, C., Steinhage, D., and Nixdorf, U.: Polar aircraft Polar 5 and Polar 6 operated by the Alfred Wegener Institute, J. Large-Scale Res. Facil., 2, https://doi.org/10.17815/jlsrf-2-153, 2016.

Wiedensohler, A., Birmili, W., Nowak, A., Sonntag, A., Weinhold, K., Merkel, M., Wehner, B., Tuch, T., Pfeifer, S., Fiebig, M., Fjäraa, A. M., Asmi, E., Sellegri, K., Depuy, R., Venzac, H., Villani, P., Laj, P., Aalto, P., Ogren, J. A., Swietlicki, E., Williams, P., Roldin, P.,

715   Quincey, P., Hüglin, C., Fierz-Schmidhauser, R., Gysel, M., Weingartner, E., Riccobono, F., Santos, S., Grüning, C., Faloon, K., Beddows, D., Harrison, R., Monahan, C., Jennings, S. G., O'Dowd, C. D., Marinoni, A., Horn, H.-G., Keck, L., Jiang, J., Scheckman, J., McMurry, P. H., Deng, Z., Zhao, C. S., Moerman, M., Henzing, B., de Leeuw, G., Löschau, G., and Bastian, S.: Mobility particle size spectrometers: harmonization of technical standards and data structure to facilitate high quality long-term observations of atmospheric particle number size distributions, Atmospheric Measurement Techniques, 5, 657–685, https://doi.org/10.5194/amt-5-657-2012, 2012.

720 Willis, M. D., Bozem, H., Kunkel, D., Lee, A. K. Y., Schulz, H., Burkart, J., Aliabadi, A. A., Herber, A. B., Leaitch, W. R., and Abbatt, J. P. D.: Aircraft-based measurements of High Arctic springtime aerosol show evidence for vertically varying sources, transport and composition, Atmos. Chem. Phys., 19, 57–76, https://doi.org/10.5194/acp-19-57-2019, 2019.

Yamanouchi, T., Treffeisen, R., Herber, A., Shiobara, M., Yamagata, S., Hara, K., Sato, K., Yabuki, M., Tomikawa, Y., Rinke, A., Neuber, R., Schumachter, R., Kriews, M., Ström, J. ., Schrems, O., and Gernandt, H.: Arctic Study of Tropospheric Aerosol and Radiation (ASTAR) 2000: Arctic haze case study, Tellus B, https://doi.org/10.3402/tellusb.v57i2.16784, 2005.

725